Two-band model for halogen-bridged mixed-valence transition-metal complexes. I. Ground state and excitation spectrum

J. Tinka Gammel, A. Saxena, I. Batistić, and A.R. Bishop
Centers for Materials Science and Nonlinear Studies and Theoretical Division, Los Alamos National Laboratory, Los Alamos, New Mexico 87545

S.R. Phillpot
Materials Science Division, Argonne National Laboratory, Argonne, Illinois 60439
(Received 23 May 1991)

We consider a $\frac{3}{4}$-filled, two-band discrete tight-binding Peierls-Hubbard model for an isolated chain of a halogen-bridged, mixed-valence, transition-metal linear-chain complex (HMMC or MX chain). We have employed the adiabatic approximation in which the quantum fluctuations associated with phonons are implicitly treated as an external field for the electrons, and treat electron-electron effects in the Hartree-Fock approximation. We investigate ground states as functions of the model parameters and doping-induced and photoinduced excitations — kinks, polarons, bipolarons, and excitons. Results for several experimental observables, including the lattice distortion, the excess charge and spin densities of defects, and the optical absorption, are compiled. For the ground state, we find that the bond-order-wave (BOW) portion of the one-band phase diagram is eliminated from the two-band phase diagram, in agreement with the lack of real materials in the pure BOW phase. The extent of electron-hole asymmetry and of spatial localization or delocalization of defects is explored. Two separate solitons or polarons are compared with corresponding bipolarons. We demonstrate explicitly the need to employ the two-band model for a realistic modeling of the MX systems, focusing on three specific systems: (a) highly distorted, valence-localized (strongly charge-disproportionated) PtCl, (b) moderately distorted PtBr, and (c) weakly distorted, valence-delocalized (weak charge-density wave) PtI. The compilation of results reported here constitutes a reference resource against which the rapidly expanding experimental data can be compared.

I. INTRODUCTION

The chemical and physical properties of low-dimensional, molecular solids have been the subject of intense study, both because of the intrinsically interesting properties of these materials and because of their important technological applications. These materials have in common both low dimensionality and competing electron-phonon (e-ph) and electron-electron (e-e) interactions. Examples of such materials are the high-temperature superconductors (e.g., $YBa_2Cu_3O_{7-\delta}$), organic superconductors [e.g., $(TMTSF)_2PF_6$, T_C=12 K], conducting polymers [the archetype of which is polyacetylene, $(CH)_x$], charge-transfer salts (e.g., TTF-TCNQ), charge-density-wave materials (e.g., $NbSe_3$), and the materials which are the focus of this study, halogen-bridged mixed-valence transition-metal linear-chain complexes (HMMC's or MX chains).

The MX chains have been of interest to chemists for many decades as strongly dichroic materials.[1] A typical crystal consists of an array of linear chains of alternating metal (M) and halogen (X) atoms; with ligands attached to the metals, and in some cases counterions between the chains to maintain charge neutrality. Symbolically, the MX complex can be represented by $[M^{\rho-\delta}L_4][M^{\rho+\delta}X_2L_4]Y_4$, where X is Cl, Br, I; M is Pt, Pd, or Ni and δ denotes deviation of valency of the transition metal ions from the average valence ρ; L is a ligand molecule such as X, ethylamine, ethylenediamine (L_2), or cyclohexanediamine (L_2); and Y is a counterion such as X or ClO_4^-, present if the chains are not neutral. In the ground state of the Ni materials there is no (or extremely weak) charge disproportionation ($\delta \simeq 0$) and no lattice distortion. In the ground state of the Pt and Pd materials, the valence dimerization of the M sublattice is stabilized by an equally strong dimerization of the X-sublattice displacements. In other words, the X atoms are displaced from the midpoint between neighboring M atoms, giving rise to charge disproportionation (mixed valence) on the M atoms, e.g., Pt^{II} or Pt^{IV} instead of the average Pt^{III}. Some examples include the ethylenediamine (en) complexes, $[Pt(en)_2][Pt(en)_2X_2]\cdot(ClO_4)_4$, hereafter referred to as PtX (X=Cl, Br, and I). The structure of the PtCl complex, shown in Fig. 1, is representative of the MX class. The major differences between members of the class being in (i) extent of lattice distortion, with PtCl, PtBr, and PtI typical of MX chains ranging from strongly to weakly distorted limit, and (ii) whether the chains are charged, as in the above examples (with Y=ClO_4^-), or neutral, as is the case for $[Pt(NH_3)_2Br_2][Pt(NH_3)_2Br_4]$. Our current modeling treats the charged and neutral chains on equal footing, based on early experimental data suggesting the structural trend (degree of distortion) depends most strongly on X. This assertion is, however, currently under study both from the experimental and theoretical viewpoints.

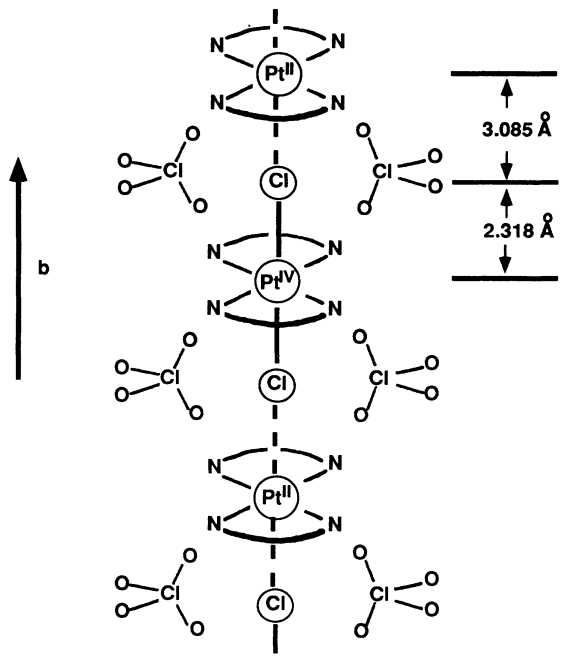

FIG. 1. Structure of the PtX material, $[Pt(en)_2][Pt(en)_2Cl_2]\cdot(ClO_4)_4$, obtained by x-ray diffraction [S.C. Huckett (unpublished)].

For the purposes of this paper, we will ignore this possible complication.

From the physicist's point of view, the potential importance of the MX class is twofold. First, the MX materials constitute a rapidly expanding *class* of near single-crystal quasi-one-dimensional systems which can be significantly "tuned": by pressure; by chemically varying M,X,L, and Y; by doping; or by using mixed metal chains, mixed halide chains, or binuclear (MMX-type) complexes instead of the pure MX chains. This tuning produces phases ranging from ones with strong M charge-disproportionation and large X-sublattice distortion (e.g., $\sim$ 20% distortion in PtCl chains) to ones with weak M charge-disproportionation and small X-sublattice distortion (e.g., $\sim$ 5% distortion in PtI chains), to ones with no apparent M charge-disproportionation or X-sublattice distortion and evidence for spin order (e.g., recently synthesized NiCl and NiBr chains[2,3]) — i.e., ground states ranging from strong charge-density-wave (CDW) to spin-density-wave (SDW) or spin-Peierls. Second, they provide the opportunity to probe doping-induced and photoinduced local defect states (nonlinear excitations such as polarons, bipolarons, kinks, and excitons) and their interactions in controlled environments over the same large range of ground states. The ability to synthesize chemically and structurally well-characterized materials which can be *controllably* tuned over a whole range of interesting phases is virtually unique among the many low-dimensional materials of current interest. Due to the increasing appreciation of the importance of strong, competing e-e and e-ph interactions in these materials, combined with the consequent need to expand many-body techniques, this ability to span a phase diagram from the CDW limit to other broken symmetry ground states enhances the potential utility of the MX chains significantly beyond that based on their pure material properties as it is critical to quantitative testing of models and methods.

The electrical conductivities of MX chains at room temperature range from values typical of insulators to those typical of small-gap semiconductors. Correspondingly, both the optical and magnetic properties vary significantly. Particularly striking is the intense dichroism resulting from the strong optical anisotropy. Raman experiments show a large resonance enhancement if the photon energy coincides with the main optical transition together with a long series of overtones for a particular phonon mode.[4] This effect is most pronounced in systems where the X atoms are displaced by a large amount from the midpoint between the M atoms, giving rise to strong charge disproportionation on the M atoms (mixed valence Pt^{II} or Pt^{IV}). In undistorted materials such as the NiCl or NiBr complexes this enhancement is expected to be very weak and may not be observable.[3] Interestingly, a pressure-induced transition from the distorted to the undistorted phase has recently been observed[5] in a PtPtBr complex, with a concomitant electronic "ionic-to-neutral" transition. Such transitions have been known to occur in mixed-stack organic charge-transfer salts, such as the tetracyanoquinodimethane (TCNQ) salts.[6] There, however, the charge disproportionation takes place on two different types of molecules, in contrast to the self-consistent mixed valence state in the halogen-bridged transition-metal complexes, and the charge disproportionation is driven by the competition between coupling to intermoleuclar and intramolecular modes. Further, most of the familiar examples of molecular chain compounds exhibit relatively weak electron-phonon coupling whereas MX compounds span from very strong coupling (e.g., PtCl) to weak coupling (e.g., PtI).

From a theoretical perspective, the MX materials represent interesting model systems with strong competitions for broken-symmetry ground states governed by e-ph and e-e interactions as well as by dimensionality, which are in many ways similar to conjugated polymers (in their chainlike structure) but which differ in some important aspects. In the polymer case the most important e-ph interaction originates from a modulation of the electronic transfer integral by the C-C stretching mode, corresponding to a coupling between the bond-order operator and the *intersite* phonons. In the MX chain the strongest e-ph coupling appears to arise from the X-X breathing mode which couples to the electronic density operator at the M atom sitting between the two X atoms. The latter resembles the coupling to *intrasite* phonons in the molecular context.[7] Due to the weak e-ph coupling in conjugated polymers the bond alternation is small (1–5%) and consequently the various types of polaronic excitations are quite extended. By contrast, in some of the MX chains the coupling to the X-X breathing mode is large and produces a strong static distortion of the X sublattice. As has been shown previously,[9] it follows that there exist highly localized electronic states, corresponding to a bound state of many phonons. The

electronic configuration associated with alternating bond lengths in the polymer case corresponds to an alternating sequence of strengthened and weakened chemical bonds, often referred to as a bond-order wave (BOW). In the MX chain, with strong coupling to the breathing mode, charge disproportionation of the M atoms occurs in the form of mixed valence which can be considered as the strong coupling limit of a CDW induced by on-site (diagonal) e-ph coupling, with an accompanying BOW on the X atoms. We chose to label this state by its M character — CDW. The competing pure BOW phase of the MX chain [BOW on the M atoms induced by intersite (off-diagonal) e-ph interactions with an accompanying CDW on the X atoms] is not observed experimentally in the MX materials. As mentioned above, in some cases (such as NiBr materials) the e-ph coupling can however be weakened to such an extent that the CDW state is completely suppressed and an (antiferromagnetic) SDW phase appears due to dominant e-e interactions for this case, possibly accompanied by spin-Peierls tendencies.

From a band-structure point of view, the MX class is essentially a hybridized two-band (M and X majority) system in which the antibonding band is half filled at stoichiometry with several nonbonding levels between the bands. The metal atoms contribute two electrons in filled d_{z^2} orbital ($\hat{z}$ is parallel to the chain) and the X atoms contribute a single electron in a half filled p_z orbital, i.e., there are six electrons per M_2X_2 unit. In the atomic limit, the electronic structure in the crystal rearranges such that the X p_z orbitals are filled and alternating oxidized (M^{4+}) and reduced (M^{2+}) metal atoms are found along the chain. (In fact, for the strongly localized PtCl materials, the spectral properties are not too different from those of oxidized and reduced monomers in solution.) In the delocalized limit (e.g., PtI), the metals are, to first approximation, in the M^{3+} state with an unpaired electron in the d_{z^2} orbital. Through the supertransfer between neighboring d_{z^2} orbitals a one-dimensional (1D) energy band is formed. This supertransfer comes from the hybridization between the d_{z^2} orbital and the p_z X orbital. Thus in an effective one-band approximation this system is expected to be a metal with a half filled energy band. Nevertheless, charge transfer does occur between neighboring M atoms due to the e-ph coupling via the Peierls mechanism,[10] and one again obtains a mixed valence (CDW) state with twice the period of original lattice:

$$-X^{-}-M^{\rho+\delta}-X^{-}-M^{\rho-\delta}-X^{-}-,$$

where the X^{-} are displaced towards the $M^{3+\rho}$. However, in contrast to the atomic limit, the charge disproportionation ρ varies with the strength of the e-ph coupling. In the limit of very weak e-ph coupling (and finite $t_\perp$) the metallic phase might be recovered, though the competing long period[11] and SDW (Ref. 12) pathways need to be considered.

Within the e-ph and e-e interaction scenario it is intriguing to note some similarities (and differences) between models and theoretical issues in MX materials and high-temperature superconducting oxides (HTSC). In cuprate HTSC e-ph and e-e interactions predominantly take place within planes spanned by Cu and O atoms. In particular, when the uppermost (fully or partially) filled O p and Cu d orbitals are included, as well as the extended Hubbard and strong (nonlinear) e-ph coupling terms, we see that at stoichiometry both systems can be described by essentially the same tight-binding extended Peierls-Hubbard Hamiltonian; although in 1D a $\frac{3}{4}$-filled, two-band model (for the MX compounds or a CuO chain), and in 2D a $\frac{5}{6}$-filled, three-band model (for the CuO planes). Thus this model, with M=Cu, X=O, is a natural description for CuO_2 planes (and chains). The analogy with 3D superconductors, e.g., $Ba_{1-x}Pb_xBiO_3$, is also quite direct.[8] Both chemical bonding and charge disproportionation have been discussed for HTSC and even proposed as likely origins for unconventional forms of superconductivity.[13] Intrinsic defects (self-trapped local defect states or bags) in both these materials are thought to be polaronic in nature, and can be created via doping or photoexcitation. Electron-hole asymmetry has been experimentally observed in MX compounds, and is perhaps important to superconductivity. Moreover, the model described below manifests long-period ("superlattice") phases, possibly observed in recent experiments on MX compounds, and may be related to twinning or real-space pairing in the cuprate HTSC. Most importantly, superconductivity occurs at the regions of "melting" between various broken symmetry ground states and correlated metals. The striking tunability of the MX *class*, along with the ease of synthesis of single crystals, will allow a close examination of competition between such phases, as well as effects of disorder and dimensionality.

The structure of a single MX chain is shown in Fig. 1, and schematically in Fig. 2. Electrons transfer preferentially along the chain while the coupling between adjacent chains is small and the ligands appear to be of mainly indirect importance for the electronic structure along the chain (e.g., affecting effective chain parameters via screening). However, three-dimensional effects cannot be always neglected. For instance, there are structural phase transitions associated with interchain order, and the average distance between two chains decreases with the application of pressure. Thus the interchain coupling must play significant role under high pressure. Indeed, the pressure dependence of optical absorption and a possible pressure-induced insulator-metal transition have been studied.[14] Since the MX chains are twofold degenerate, domain walls (solitons) are likely to be present. The soliton mass in PtCl chains[33] has been estimated to be several hundred times as much as in *trans*-$(CH)_x$.[15] This suggests that solitons (and other excitation species) in valence localized MX chains are far less mobile than in *trans*-$(CH)_x$. Thus, upon photoexcitation, if the photogenerated carrier pairs become widely separated before self-localizing, they will have a long lifetime since their effective masses are then too heavy to allow the necessary movement for recombination. Such long-lived photoinduced absorption and photoinduced electron spin resonance (ESR) in PtCl complexes have been observed when photoexcitation was made in the region of the intervalence charge-transfer (IVCT) band or above.[16,17]

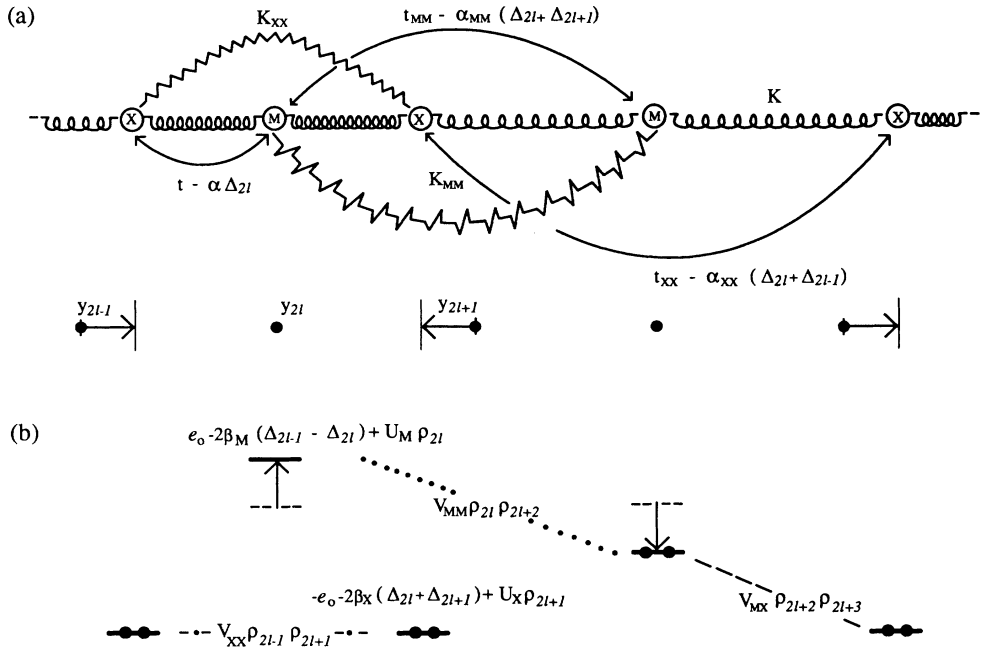

FIG. 2. (a) Schematic of the MX chain showing the model parameters and a CDW distortion; (b) the corresponding $t_0=\alpha=0$ energy levels.

The absorption and ESR are induced only for the excitation with light polarized parallel to the chain axis, and the photoinduced absorption is polarized parallel to the chain, suggesting that the photogenerated carriers are located on single chains. For the more delocalized MX chains, the carrier masses are not expected to be as heavy: the electrical conductivity of a halogen-doped PtI complex has been reported to increase by seven orders of magnitude.[18]

The study of CDW's in MX complexes can be to great advantage since one has several kinds of crystals with similar structures. Further, there is the additional richness which can be probed by studying the variation in heterometal halide ($M_xM'_{1-x}X$), metal heterohalide ($MX_xX'_{1-x}$), and bimetallic halide (M_2X) complexes.[19,20] The relationship between the electronic and structural properties has been extensively studied by absorption, reflection, electrical conductivity, luminescence, resonant Raman, electroreflectance, ESR, and x-ray appearance near-edge structure (XANES) experiments.[1,16–18,21–25] As noted above, the band gap, E_g, and lattice distortion, Δ, tend to vary systematically with the choice of M and X. As M varies from Pt→Pd→Ni, the atomic radius of the metal M (r_M) decreases. As X varies from Cl→Br→I, the radius of X (r_X) increases. The decrease of r_M increases the intraorbital Coulombic repulsion on a metal site, U_M, and decreases the supertransfer energy (or hopping integral) between metal ions, t_0. The increase of r_X enhances t_0. Increased U_M or t_0 leads to the reduction of the CDW lattice distortion amplitude Δ, if the e-ph interaction is unaltered. This agrees with the observed experimental trend: the strength of CDW distortion decreases with M varying from Pt→Ni and X varying from Cl→I. In NiCl or NiBr, the Peierls distortion is absent because of the larger Coulombic repulsion of Ni. (The NiX are in a SDW state, which opens up the further advantage of the MX class of materials of being able to study transitions between competing ground states.) Decreased Δ leads to a reduction in the Peierls contribution to E_g again agreeing with the trend observed for the optical gap as X is varied in, e.g., the PtX materials. However, as M is varied from Pt→Ni, the reduction in E_g due to the reduction in Δ can be offset by the increase in U_M. Thus the optical gap is not expected to decrease as fast as the lattice distortion, and might even increase. There is less experimental data available on the Ni materials, though it appears that E_g tends to decrease slightly.

The above discussion strongly indicates that the MX class of materials not only provides a 1D paradigm but also serves as a testing ground for experimental techniques and theoretical concepts in many-body, strongly interacting (both e-e and e-ph), low-dimensional electronic materials. The advantage of chemical tuning and single crystals further emphasizes the need for, and merit of, a systematic, comparative study to utilize efficiently these special-purpose materials. The work described in this paper is part of a joint theoretical effort to provide a unified understanding of these materials from the different many-body viewpoints of band-structure calculations[26] valid in the delocalized limit, *ab initio* quantum-chemistry calculations[27] valid in the highly localized limit, and tight-binding model calculations as presented here, which should be valid throughout the range, with parameters derived from these two other sources and/or experiment.

In the next section we present the model Hamiltonian. Section III describes the properties of the ground state,

while the general properties of the spectrum of defect states (doped and photoexcited) are described in Sec. IV. We compile results for total energy, energy levels, excess charge and spin densities, dimerization pattern, CDW, BOW and optical absorption for various nonlinear excitations that can occur in each one of these three systems, either intrinsically, or by photoexciting, or as a result of doping. The excitations include neutral, positively and negatively charged kinks (solitons), polarons and bipolarons. In addition, two nearby as well as two separate solitons and polarons are also considered on a chain. Such a comparative study provides insight into the nature of the e-ph coupling and other parameters that govern the Hamiltonian. This compilation of results also provides a reference resource for comparisons with experimental data. To emphasize this contact with experiment, we focus on the theoretical study of nonlinear excitations in three specific systems: X=Cl, Br, I in the PtX complexes $[Pt(en)_2][Pt(en)_2X_2]\cdot(ClO_4)_4$. This study compares the behavior of these excitations in a strongly localized regime (PtCl) with that of a very delocalized regime (PtI). PtBr represents an intermediate regime. Further, by retaining an X atom electronic orbital explicitly we stress the need and validity of a two-band model. The present model is analogous to a model for ordered AB polymer[28] but, importantly, with $\frac{3}{4}$-band filling (half a hole per site). Further, this model has no electron-hole symmetry or, in general, reflection plane symmetry (though defects tend to retain the reflection symmetry of the ground state about a metal ion, when topologically possible). In Sec. V, we summarize the salient features of our study and conclude with some comments on MX systems with M and X fixed or variable (mixed-halide, $MX_xX'_{1-x}$, and mixed-metal, $M_xM'_{1-x}X$, systems), as well as MMX systems. In particular, comparison of MX XPS data with $M_xM'_{1-x}X$ data indicates that M' causes an additional modulation of the mixed-valence states,[29] and hence a considerable modification of the electron-transfer mechanism (supertransfer in a one-band model). Brief reports of part of this work have appeared previously.[30]

II. MODEL AND HAMILTONIAN

Many previous tight-binding models for the MX materials have included only the electrons on the M atoms,[9,31–33] as the difference between the X and M atom on-site affinities ($2e_0$) is large in the more common MX complexes. Here, as in Ref. 30, we retain an X atom electronic orbital explicitly in order to (i) study systematically the effects of having two kinds of atoms in the chain, and (ii) investigate the experimental signatures which indicate when the $\frac{1}{2}$-filled one-band approximation is valid and when not. (We do not, however, include the nonbonding orbitals — though a multiband formalism could be similarly formulated to investigate the effects of retaining them, were it thought necessary.) We are also interested in the small e_0 limit for strongly hybridized systems, where M-X hybridization cannot be neglected and a $\frac{3}{4}$-filled two-band model *must* be used. (This limit may also be relevant to, e.g., the superconducting oxides.) Focusing on a single orbital per site and including only nearest neighbor M-X, X-X, and M-M interactions, we use the following two-band tight-binding model for the isolated MX chain:[30]

$$H = H_{e\text{-ph}} + H_e + H_{\text{ph}} + H_{\text{ext}} , \tag{1}$$

where

$$\begin{aligned} H_{e\text{-ph}} = & \sum_{l,\sigma}\{(-t_0+\alpha\Delta_l)(c^\dagger_{l,\sigma}c_{l+1,\sigma}+c^\dagger_{l+1,\sigma}c_{l,\sigma}) + [\epsilon_l-\beta_l(\Delta_l+\Delta_{l-1})]c^\dagger_{l,\sigma}c_{l,\sigma}\} \\ & + \sum_{l,\sigma}\{[-t_{MM}+\alpha_{MM}(\Delta_{2l}+\Delta_{2l+1})](c^\dagger_{2l,\sigma}c_{2l+2,\sigma}+c^\dagger_{2l+2,\sigma}c_{2l,\sigma}) \\ & + [-t_{XX}+\alpha_{XX}(\Delta_{2l-1}+\Delta_{2l})](c^\dagger_{2l-1,\sigma}c_{2l+1,\sigma}+c^\dagger_{2l+1,\sigma}c_{2l-1,\sigma})\} , \end{aligned} \tag{2a}$$

$$H_e = \sum_l U_l n_{l\uparrow}n_{l\downarrow} + V_{MX}\sum_l n_l n_{l+1} + V_{MM}\sum_l n_{2l}n_{2l+2} + V_{XX}\sum_l n_{2l-1}n_{2l+1} , \tag{2b}$$

$$H_{\text{ph}} = \frac{1}{2}\sum_l \frac{\hat{p}_l^2}{M_l} + \frac{1}{2}K_{MX}\sum_l \Delta_l^2 + \frac{1}{2}K_{MM}\sum_l(\Delta_{2l}+\Delta_{2l+1})^2 + \frac{1}{2}K_{XX}\sum_l(\Delta_{2l-1}+\Delta_{2l})^2 , \tag{2c}$$

$$H_{\text{ext}} = P\sum_l \Delta_l + \sum_{l,l'} W_{\text{ext}}(l,l')\,n_{l'} . \tag{2d}$$

We use the convention that M atoms sit on even sites, X atoms on odd sites. Thus $\varepsilon_l = [\varepsilon_X, \varepsilon_M] = [-e_0, +e_0]$, $\beta_l = [\beta_X, \beta_M]$, $U_l = [U_X, U_M]$, and $M_l = [M_X, M_M]$, for l = [odd, even] respectively. We define the relative coordinates $\Delta_l \equiv \hat{y}_{l+1} - \hat{y}_l$, where $\hat{y}_l$ are the displacements from uniform lattice spacing of the atoms at site l with mass M_l and momenta $\hat{p}_l$. The number operator is given by $n_{l,\sigma} = c^\dagger_{l,\sigma}c_{l,\sigma}$, where $c^\dagger_{l,\sigma}$ ($c_{l,\sigma}$) creates (annihilates) an electron in the Wannier orbital at site l with spin σ. At stoichiometry there are six electrons per

unit cell (M_2X_2 unit), and the model has $\frac{3}{4}$ filling. The model parameters are shown schematically in Fig. 2. In Eq. (2a), we model the difference in (on-site) energies of M d_{z^2} and X p_z orbitals on isolated atoms by $2e_0$ [$-e_0$ on X (odd) sites, $+e_0$ on M (even) sites]. The hopping between these levels is modeled by t_0. Two different e-ph couplings are included: the dependence of the hopping integral on distance (α) and the coupling of the on-site energy to the breathing mode of its neighbors along the chain (β_M, β_X). In general, we also include the possibility of distance dependent M-M (t_{MM}, α_{MM}) and X-X (t_{XX}, α_{XX}) hopping. In Eq. (2b), the e-e interaction is modeled by including on-site, NN and NNN Hubbard terms ($U_M, U_X, V_{MX}, V_{MM}, V_{XX}$). Longer-range coupling to a Madelung term, especially in the strong CDW regime, is also under investigation.[34] All other intrinsic interactions (core-electron repulsion, ligand-ligand interaction, etc.) are lumped into the effective spring terms (K, K_{MM}, K_{XX}) given in Eq. (2c). $H_{\rm ext}$, Eq. (2d), is included to model the possibility of an external pressure P, which couples to the total length of the MX chain, and an external potential $W_{\rm ext}$ (such as pinning centers or periodic potential due to the neighboring chains), which couples to the site density. We have also adjusted the pressure, or, equivalently, constrained the distortion, so that the sum of the atomic displacements is zero. This is not strictly necessary, but omitting this constraint just shifts the chemical potential and renormalizes the hopping integral: $t_0 \rightarrow t_0 - \alpha\Delta_0$, where $\Delta_0 = (1/N)\sum_n \Delta(n)$. The effective parameter values to compare with experiment were determined using this constraint.

To ensure approximation-independent results we have employed a variety of theoretical techniques to study the ground and defect states for the many-parameter model, Eq. (1). These include the $t_0 \rightarrow 0$ localized limit, both weak- and strong-coupling perturbation theory, Hartree-Fock (HF) approximation, exact diagonalization and quantum Monte Carlo on small clusters, variational *Ansätze* including quantum phonons, and adiabatic molecular dynamics. In the present context we focus on the HF, adiabatic results, and note that quantum phonon corrections are inconsequential for the heavy atoms considered here. The effects of including quantum phonons and e-e correlations via Hubbard terms are described in a companion article,[12] hereafter referred to as paper II, and the work presented here should be considered as using HF effective $U=0$ parameters. The HF results have been calibrated against exact results obtained using a Lanczos diagonalization procedure,[35] and essentially no difference was observed in the CDW phase for small to intermediate correlations.[30] This contrasts sharply with the half filled band, BOW case of polyacetylene, where, e.g., the dimerization amplitude is independent of the Hubbard U in HF approximation (the first-order corrections are zero for perturbation in U) but the dimerization amplitude is strongly dependent on the Hubbard U in exact calculations.[36] For the discussion in the rest of the paper we set the NNN hoppings, X-X spring, Hubbard terms, and external potential to zero, and consider only adiabatic phonons. Thus the general Hamiltonian (1) reduces to the more tractable form:

$$\begin{aligned} H &= \sum_{l,\sigma}\{(-t_0+\alpha\Delta_l)(c^\dagger_{l,\sigma}c_{l+1,\sigma}+c^\dagger_{l+1,\sigma}c_{l,\sigma}) \\ &\quad + [(-1)^l e_0 - \beta_l(\Delta_l+\Delta_{l-1})]c^\dagger_{l,\sigma}c_{l,\sigma}\} \\ &\quad + \frac{1}{2}K\sum_l \Delta_l^2 \\ &\quad + \frac{1}{2}K_{MM}\sum_l(\Delta_{2l}+\Delta_{2l+1})^2 , \end{aligned} \tag{1'}$$

where the subscript has been dropped on K_{MX} for simplicity. As shown below, for the HF effective ($U=0$) parameter sets, the ground state is always a CDW state. For $U\neq 0$, we can define effective $U=0$ parameters such that the same uniform band structure results for a given distortion. U_M is anticipated to be of the order of 1–2 eV for PtX materials. For NiX, U_M is expected to be substantially larger, driving the SDW phase. The reduced-parameter Hamiltonian (1′) leads to the following self-consistency equation for lattice distortion:

$$\overline{K\Delta_l} = -\alpha_l\sum_\sigma\langle c^\dagger_{l,\sigma}c_{l+1,\sigma}+\text{H.c.}\rangle + \beta_l\langle n_l+n_{l+1}\rangle , \tag{3}$$

where

$$\begin{aligned} \overline{K\Delta_l} &= K\Delta_l + K_{MM}(\Delta_l+\Delta_{l-1})\delta_{l,\text{odd}} \\ &\quad + K_{MM}(\Delta_l+\Delta_{l+1})\delta_{l,\text{even}} . \end{aligned} \tag{4}$$

For a given distortion Δ_l, the electronic parts of the Hamiltonian are numerically diagonalized to find the electronic eigenvalues and eigenfunctions. The self-consistency condition is then used to generate the next approximation to the minimum energy lattice distortion. The procedure is iterated until this approximate distortion changes by a given (infinitesimal) amount, i.e., the distortion has converged to numerical accuracy. The optical absorption of the resulting configuration was calculated using the Fermi golden rule

$$\alpha(\omega) = \frac{\pi}{\omega}\sum_{f,i}|\langle f|J|i\rangle|^2\delta(\omega-e_f+e_i) , \tag{5}$$

and Lorentzian broadened. Here f, i denote the final and initial states and J the current operator

$$J = i\sum_{\ell,\sigma}(-t_0+\alpha\Delta_\ell)(c^\dagger_{\ell,\sigma}c_{\ell+1,\sigma}-c^\dagger_{\ell+1,\sigma}c_{\ell,\sigma}) . \tag{6}$$

Calculations were typically done on lattices of less than 100 sites, though for the more delocalized materials (e.g., PtI) lattices of up to 400 sites were used as needed to remove most of the artificial oscillations in the spectra introduced by this finite chain procedure. We have also explored the relaxation to the final state, using the molecular-dynamics technique described in Appendix A.

To explore the parameter dependence of the model, we have used the dimensionless parameters defined in Table I. Energies are scaled by $2t_0$ and distances by t_0/α. Values cited in the rest of this paper are the dimensionless ones unless otherwise noted. The parameter

TABLE I. (a) Model parameters, (b) the corresponding dimensionless parameters, (c) the effective one-band parameters for large e_0 (but see Appendix B), and (d) the effective U=0 parameters that give the same band structure as the bare parameters with U, assuming a CDW. Here $\rho_{M\,(X)}$ is the average charge on the $M(X)$ sites, and $2\delta\rho_M$ is the difference in charge of the inequivalent metal atoms. Note that the entire two-band phase diagram for positive $\beta_M = \beta_X = \beta$ and e_0 maps into only the CDW part of the one-band phase diagram, but U can cause a negative β, reintroducing the BOW phase.

(a)	H	t_0	α	e_0	β	K	Δ
(b)	$\frac{H}{2t_0}$	$\frac{t_0}{2t_0}$	$\frac{\alpha}{2\alpha}$	$\frac{e_0}{2t_0}$	$\frac{\beta}{2\alpha}$	$\frac{Kt_0}{2\alpha^2}$	$\frac{\alpha\Delta}{t_0}$
(c)	H	$\frac{t_0^2}{2e_0}$	$\frac{\alpha t_0}{2e_0}$	(∞)	$\beta + \frac{\alpha t_0}{e_0}$	K	Δ
(d)	$H + \langle\hat{U}\rangle$	t_0	α	$e_0 + \frac{U_M\rho_M - U_X\rho_X}{4}$	$\beta_M - \frac{U_M\delta\rho_M}{4\Delta}$	$K - \frac{U_M\delta\rho_M^2}{4\Delta^2}$	Δ

values appropriate to PtX materials, listed in Table II, were determined from comparison to *ab initio* quantum chemistry[27] and band-structure calculations,[26] and from comparison to ground-state experimental information [namely the X-sublattice distortion amplitude (Δ), the IVCT band edge or optical gap (E_g), and the $\sigma(X) \rightarrow d_\sigma^*$ absorption for the oxidized monomer]. The *ab initio* and band-structure calculations were performed for $[Pt(NH_3)_2Br_2][Pt(NH_3)_2X_4]$ materials as (i) the chains are charge neutral so no counter-ions between chains are present; and (ii) the $(NH_3)_2Br_2$ ligands are small and thus there are a minimum number of atoms in the unit cell. As we expect interligand interactions to strongly constrain the metal-metal distance, we focus on $K_{MM} \rightarrow \infty$ when discussing the defects. We have studied the model for finite K_{MM} and found that for $K_{MM} \simeq K$ the results differed negligibly from $K_{MM} \rightarrow \infty$. The present parametrization is only representative. More experimental data are needed for unambiguous parameter determinations.

In the large e_0 limit, this model can be related to the one-band model developed by Baeriswyl and Bishop,[9] as shown in Appendix B. The values of the one-band parameters appropriate to PtX are also listed in Table I. Baeriswyl and Bishop[9] determined that for $(\beta^{1b})^2/(2\alpha^{1b})^2 > 1$, the ground state is a CDW. From Appendix B we find that

$$\frac{(\beta^{1b})^2}{(2\alpha^{1b})^2} = \frac{[\beta_M + (\frac{\alpha t_0}{e_0})]^2}{(\frac{\alpha t_0}{e_0})^2} > 1. \quad (7)$$

Thus we see that the two-band model for $e_0 > 0$ and $\beta_M > 0$ maps to *only* the CDW part of the one-band phase diagram. The two-band model thus explains why the BOW phase is never observed experimentally, even in materials where the ligands are small and thus the M-M spring, K_{MM}, is expected to be weak.

III. GROUND STATES

The general model has been found to be capable of supporting several ground states: period-4 CDW, SDW, BOW, spin-Peierls, as well as intriguing long-period (superlattice) patterns. As discussed above, the effective one-band parameters are such that the ground state is *always* in the CDW part of the phase diagram. Because the values of K_{MM} and β_X do not affect the CDW ground state, to reduce the number of parameters and to explore the possibility of a BOW phase, we have set $\beta_X = \beta_M = \beta$ and $K_{MM} = 0$ in the ensuing discussion of the *ground* states. Since we expect this model to be applicable to many systems, we explore the phase diagram over a wide range. In particular, we examine small e_0, where strong hybridization occurs.

TABLE II. Dimensionless parameters for the PtX materials from comparison to *ab initio* calculations (Ref. 27). These numbers are scaled to match ground-state experimental data (optical gap, lattice distortion amplitude) on PtCl (Refs. 25 and 30), as the IVO (improved virtual orbital) corrections to the *ab initio* calculations are still in progress. These numbers are to be interpreted as effective U=0 mean-field values.

			Dimensionless				
MX	$t_0/2t_0$	$\alpha/2\alpha$	$e_0/2t_0$	$\beta_M/2\alpha$	$K_{MX}t_0/2\alpha^2$	$\alpha\Delta/t_0$	$E_g/2t_0$
PtCl	0.5	0.5	0.3	0.030	0.524	0.6	0.812
PtBr	0.5	0.5	0.2	0.035	0.695	0.4	0.579
PtI	0.5	0.5	0.1	0.040	1.019	0.2	0.301

			Actual value				
	t_0 (eV)	α (eV/Å)	e_0 (eV)	β_M (eV/Å)	K_{MX} (eV/Å^2)	Δ (Å)	E_g (eV)
PtCl	1.54	2.38	0.924	0.143	3.91	0.38	2.5
PtBr	1.30	2.17	0.520	0.152	5.03	0.24	1.5
PtI	1.99	2.65	0.398	0.212	7.19	0.15	1.2

A. Period 4

The Hamiltonian given in Eq. (1) may be analyzed analytically to give the ground state. A general period 4 lattice distortion Δ_l can be written as

$$\Delta(l) = (-1)^l d + \Delta \cos\theta \left(\cos\frac{\pi l}{2} + \sin\frac{\pi l}{2}\right) + \Delta \sin\theta \left(\cos\frac{\pi l}{2} - \sin\frac{\pi l}{2}\right) . \quad (8)$$

We expand the wave function in Bloch states

$$\psi_k(l) = \left(A + (-1)^l B + C \cos\frac{\pi l}{2} + D \sin\frac{\pi l}{2}\right) e^{ikla}, \quad (9)$$

where a is the lattice spacing, $-\pi/2 < ka \leq \pi/2$, and A, B, C, and D are to be determined. The total energy of the system is given by (recall $K_{MM} = 0$)

$$E_{\text{total}} = \sum_{k,\sigma \text{ occ}} E_{k,\sigma} + \tfrac{1}{2} K \sum_l \Delta^2(l) , \quad (10)$$

where $E_{k,\sigma}$ are the single-particle electronic energies. For $d \neq 0$, it can be shown that the total energy is raised, thus we set it to zero, yielding for a mixed CDW/BOW phase the following eigenvalue equation for E_k:

$$\left[E_k^2 - e_0^2 - 2(t_0^2 + \alpha^2\Delta^2)\right]^2 = 4\cos^2 ka (t_0^2 - \alpha^2\Delta^2)^2 + 4\Delta^2\left[\beta(E_k + e_0) + 2\alpha t_0\right]^2 - 4\Delta^2\cos^2\theta\beta e_0(\beta E_k + 2\alpha t_0) - 4\Delta^4 \sin^2 2\theta \left((\beta^2 - \alpha^2)^2 - \alpha^4 \sin^2\frac{ka}{2}\right) . \quad (11)$$

It immediately follows that Eq. (10) depends only on Δ^2 [or equivalently, $E_{\text{total}}(\theta) = E_{\text{total}}(\theta + \pi)$], and thus the ground state will be at least doubly degenerate. We see that for $\beta = 0$ or $e_0 = 0$ the above equation depends only on 2θ, and the CDW and BOW are isoenergetic. Analyzing the θ dependence of the total energy, it can be shown that the third term on the right-hand side of Eq. (11) raises the energy if $\cos\theta \neq 0$. The fourth term also raises the total energy for $\sin^2(2\theta) \neq 0$, unless

$$\left[(\beta^2 - \alpha^2)^2 - \alpha^4 \sin^2\left(\frac{ka}{2}\right)\right] < 0 . \quad (12)$$

Thus the CDW is preferred ($\theta = \pi/2$), except in a small region near $e_0 = 0$ and $\beta = \alpha$. The band structure at fixed β as a function of e_0 for two different Δ is shown in Fig. 3.

From Eq. (11) we find for the location of the edges of the top and bottom energy gaps [$\cos(ka) = 0$]:

$$E_{I,J} = I\beta\Delta + J[2(t_0 + I\alpha\Delta)^2 + (e_0 + I\beta\Delta)^2]^{1/2}, \quad (13)$$

where $I, J = \pm 1$ independently to give the four eigenvalues. Assuming narrow bands (appropriate to PtCl) so that $E(k) \simeq E(\pi/2a)$, we obtain a simple formula for K

$$K = \frac{\beta}{4\Delta} + \frac{1}{4\Delta} \frac{2\alpha(t_0 + \alpha\Delta) + \beta(e_0 + \beta\Delta)}{[\,2(t_0 + \alpha\Delta)^2 + (e_0 + \beta\Delta)^2\,]^{1/2}} \quad (14)$$

and find that K has a maximum as a function of e_0 at $\beta/2\alpha \simeq e_0/2t_0$. This maximum does not appear to be important for any of the physical properties of the system. From Eq. (14), we also deduce that the amplitude of the CDW increases linearly with β for large β. Further analyzing Eq. (11), we see that for small e_0, the splitting due to α and/or β dominates and the bands are ordered from top to bottom $MXXM$ [where M (X) denotes the bands have more than 50% $M(X)$ character]. As e_0 increases, the band ordering shifts to $MXMX$. Finally, the splitting due to e_0 dominates and the band order is $MMXX$. The phase boundaries and amplitude of the lattice distortion are nearly independent of system size for $N \geq 16$. The resulting phase diagram, shown in Fig. 4, is rather featureless, even for $K_{MM} = 0$, the ordering of the hybridized band character being the only major feature. The band character changes roughly where the band edges cross. The lower gap closes when

$$\frac{e_0}{2t_0} = \frac{1}{2}\frac{\beta}{2\alpha}\left[1 + \left(\frac{\alpha\Delta}{t_0}\right)^2\right] - \frac{1}{4}\frac{1}{\beta/2\alpha} \quad (15)$$

and the middle gap closes when

$$\frac{e_0}{2t_0} = 2\frac{\beta}{2\alpha}\frac{\alpha\Delta/t_0}{1 + (\alpha\Delta/t_0)^2} . \quad (16)$$

This simple analysis, based merely on the locations of the band-edge crossings is borne out by numerical investigation of the M,X character of the full bands, as seen by comparing the actual phase boundaries with the locations of the band crossings in Figs. 3 and 4. The transition from the $MXXM$ to the $MMXX$ phase seems to be in between the point where the bands cross and the point for which the band edges in Eq. (11) for $I = -1$ have an extremum ($e_0 = \beta\Delta$) — also marked in the figures. Furthermore, as discussed above, the BOW appears only for an extremely small region near $e_0 = 0$ and $\beta = \alpha$ where the lowest energy state is of mixed BOW-CDW character. This is in agreement with the fact that all known MX materials with structural distortion are in the CDW phase, and demonstrates one important difference between the two-band model and one-band models,[9] where the BOW phase is found for a substantial range of parameter values.

The "relative strength" of α and β may be determined from Eq. (13). We find that (α, β=0) and (α=0, β) yield the same electronic gap if

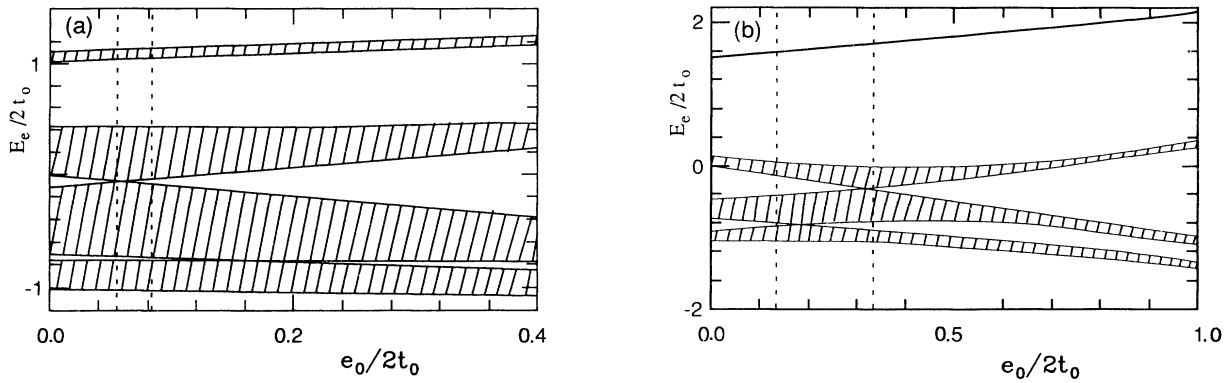

FIG. 3. Energy bands as a function of e_0 for $t_0 = 0.5$, $\alpha = 0.5$, and $\beta = 0.8$ for (a) $\Delta = 0.2$ and (b) $\Delta = 0.5$. The phase boundaries from Fig. 4 are indicated. Note that they roughly correspond to the band-edge crossings.

$$\frac{2\alpha}{\beta} = \frac{e_0}{2t_0} + \left[\frac{1}{2} + \left(\frac{e_0}{2t_0}\right)^2\right]^{1/2}. \quad (17)$$

Thus for small e_0 the same gap is obtained for $\alpha \simeq \beta$, whereas for large e_0 the same gap is obtained for $\alpha >> \beta$. We have also examined $\beta < 0$. (The Hubbard U term acts in mean-field approximation like a negative β. See Table I and paper II.) There one finds a BOW with amplitude approaching zero as the system size increases for small to intermediate negative β, and a CDW with increasing amplitude for large negative β. Note that the parameters for $U > 0$ are discussed in paper II.

B. Long period

While Peierls's theorem[10] guarantees that a commensurate distortion is lower in energy than no distortion in one-dimensional e-ph coupled systems, it does not rule out the possibility that another distortion will be even lower in energy. Interestingly, we have found that for this model with $K_{MM} = 0$, the on-site e-ph coupling (β term) drives a long-period phase even at *exactly* commensurate filling.[11] To see this consider the trivial zero-hopping limit (t_0=α=0) where the electronic Hamiltonian is site-diagonal and the eigenstates are fully described by their site occupancy (0, 1, or 2). The period 4 phase is then

$$\cdots XMX\,M\,XMX\,M\cdots = \cdots 202\,2\,202\,2\cdots.$$

It is easy to show that the lowest energy state for small e_0 phase separates into two regions, one of which has all the sites fully occupied and one of which has all the sites empty:

$$222\cdots 222000\cdots 0.$$

The hopping drives the competing period 4 phase. Our numerical investigations indicate that there are many (metastable) long-period phases for finite t_0. A roughly period-10 distortion, lower in energy than the period-4 phase, is shown in Fig. 5. Note that this phase resembles a (spontaneously generated) soliton-antisoliton lat-

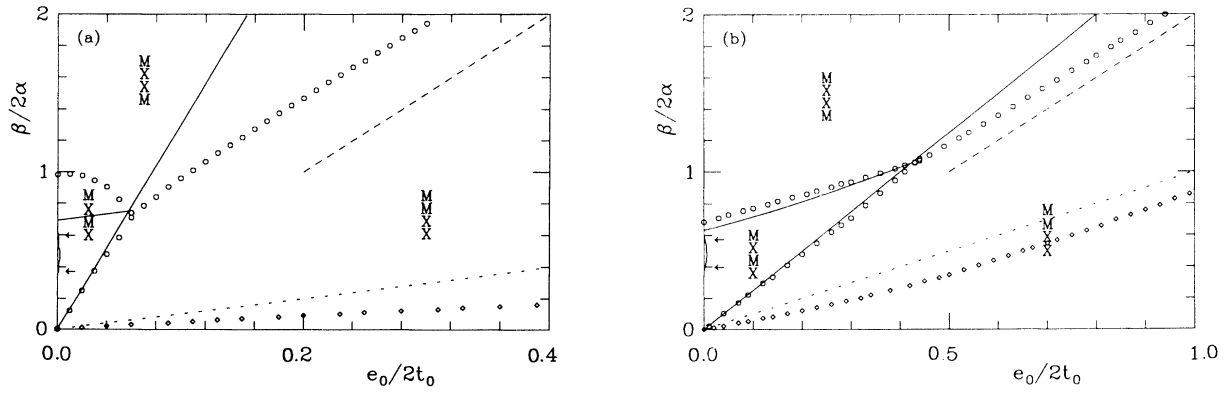

FIG. 4. Period 4 phase diagram at constant Δ for (a) $\Delta = 0.2$ and (b) $\Delta = 0.5$. Note that the scales are different. The CDW regions are labeled by the ordering of the hybridized bands. The solid lines mark the boundaries predicted by examining the gap edges crossings, the long-dashed line marks the boundary predicted by examining the band-edge maximum, and the circles mark the boundaries found numerically. These transitions are not sharp, and the regions near the boundaries can have, e.g., one-band predominantly $M(X)$, with the other three bands slightly $X(M)$ in character. The value of K needed for Δ to be self-consistent is predicted to be maximum as a function of e_0 on the dotted line; diamonds mark the numerical result. The narrow region of mixed CDW and BOW distortion near the β axis, found numerically, is marked by arrows.

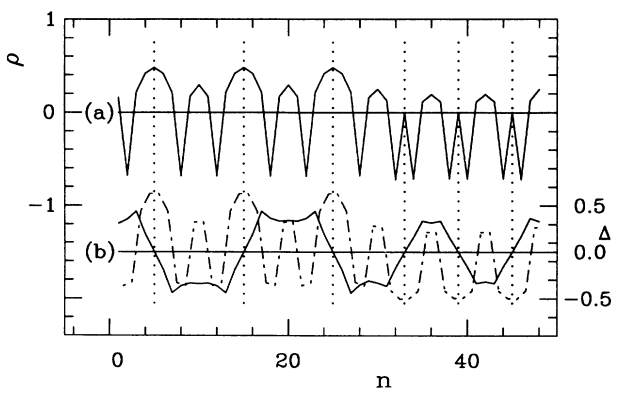

FIG. 5. A long-period distortion at exactly commensurate filling, which is roughly a soliton lattice of period 10. Shown are (a) the charge density and (b) the CDW lattice distortion order parameter (solid). The actual lattice distortion is also shown for comparison (dashed), and the centers of the solitons are marked by dotted vertical lines. This long-period distortion is lower in energy than the period-4 phase by $\simeq 2\%$ of the energy gain over the undistorted phase. Parameter values are $t_0 = 1$, $\alpha = 0$, $e_0 = 0.5$, $\beta_{M,X} = 0.7$, and $K = 1$.

tice. We investigate these long period phases in detail in Ref. 11. STM experiments to look for long-period phases in MX and MMX materials are currently in progress.[37] We speculate that this tendency toward charge-clumping may be related to twinning (superlattice discommensurations), or real-space (bipolaronic) pairing in the 2D extension of our model. However, in the rest of this paper we consider only the ground state in, and localized defects with respect to, the period-4 phase.

IV. LOCALIZED INTRAGAP STATES AND OPTICAL ABSORPTIONS

We investigated the excitation spectrum of our model in the absence of correlations using a numerical adiabatic relaxation code (see Appendix A and Ref. 38) to quench an initial condition until the force on each atom reached a fixed small value. Equivalently, we iteratively solved for the static lattice distortion until we produced solutions that were self-consistent to numerical accuracy. Using both methods was important, as in the molecular relaxation code, the CDW distortion relaxes quickly, while the forces driving the BOW away from zero distortion are small; whereas the self-consistent code easily finds the local BOW distortion. Conversely, the self-consistent code is not useful for distinguishing in the valence-trapped limit between a close kink pair and a bipolaron (bound kink pair); whereas the molecular relaxation code is useful for examining this discrete lattice dichotomy. In the $\frac{3}{4}$-filled CDW ground state, the cases of one and two added or subtracted electrons on a ring of length $N=4n$ (polarons, and bipolarons or kink pairs) and zero and one added or subtracted electron on a ring of length $N=4n+2$ (neutral and charged kinks) were studied. For most results reported here chains of length 48, 60, and 200 were used for PtCl, PtBr and PtI, respectively (the more delocalized, the longer the chain required for the discrete level spacing to be small compared to other energies in the problem). For odd numbers of kinks the corresponding chain lengths were 50, 62, and 198. Lattices up to 400 sites were studied to test finite-size dependence. In our calculations, $4n$ ($4n+2$) sites correspond to $Pt^{3-\delta}$ ($Pt^{3+\delta}$) [Pt^{II} (Pt^{IV}) in the strong CDW limit]. Low- to high-density defect lattices (from one defect per chain up to the defect width equaling the defect spacing) were studied by enforcing Bloch periodicity on short chains (of length N) with a single defect to simulate longer chains (of length $N' = mN$) with a lattice of (m) defects. The effects of missing halides and external pinning potentials were also studied. Periodic-boundary conditions were employed. Other boundary conditions, such as antiperiodic and open chain, were also used in certain test cases and did not seem to affect the results in any significant manner, except to tend to center the defects at, or maximally away from, the boundary. In addition, for a discrete system the lattice distortions and absorption frequencies depend on where the defect is centered; we report only the lowest energy results (this discreteness pinning can be significant, especially in PtCl where the defects are localized over only a few sites).

When the M-M distance was allowed to vary (i.e., K_{MM} was finite), the CDW distortion for the various cases was accompanied by a localized BOW distortion, which followed essentially the derivative of the CDW distortion. (This is somewhat analogous to including acoustic and optic phonons in polyacetylene models.[39]) For $K_{MM}=0$ this local BOW amplitude is of the same order of magnitude as the CDW distortion amplitude. As K_{MM} increases, the local BOW amplitude decreases. When $K_{MM}\to\infty$ there was, of course, no BOW distortion and the CDW distortion was slightly more spread out. We found that for the experimental parameter set $K_{MM} \simeq K$ differed negligibly from $K_{MM}\to\infty$. We focus on the two limiting cases as the behavior appears to vary smoothly with K_{MM}, as discussed below.

A. Defect states: Trends

1. Location of excitations. Since the CDW in MX chains has periodicity 4, the ground state location of an excitation on the chain is sensitively dependent on its charge, and on the chain length. For example, an odd number of kinks must be present if the chain has length $N=4n+2$. There is also the usual Jahn-Teller, non-Jahn-Teller dependence ($N=8n$ vs $N=8n+4$), which vanishes in the limit of long chains. Since the ground state is doubly degenerate, to discuss locations we need to specify the configuration of the ground state. The ensuing discussion assumes that the ground state has the following symmetry:

$$\cdots X\text{-}M\text{-}X\text{—}M\text{—}\cdots,$$

i.e., (short, short, long, long) bonds at ($4n+1$, $4n+2$, $4n+3$, $4n+4$) sites, respectively. Positively charged polarons (P^+) are seen to be located on $4n$ sites while electron polarons (P^-) prefer $4n+2$ sites. Bipolaron location

depends on whether n is even or odd. For n even, neutral and negative bipolarons (B^0, B^{2-}) are located at $4n+2$ sites while the hole bipolaron (B^{2+}) resides on $4n$ sites. For n odd, the situation is reversed; neutral and electron bipolarons prefer $4n$ sites while hole bipolaron resides on $4n+2$ sites. In the case of topological defects such as kinks, across the defect the ground state undergoes a 180° phase shift (reverses in sign), thus one must define both "left" ($x < x_d$) and "right" ($x > x_d$) reference phases. We have chosen the rightmost phase ($x \to \infty$) to be the one pictured above. Thus for an odd number of kinks the chain will start out in the oppositely configured ground state, i.e., sites 1–4 are:

$$\cdots X\text{—}M\text{—}X\text{-}M\text{-}\cdots \ .$$

For $N=4n+2$ neutral and electron kinks (K^0, K^-) are found to be located (centered) on $4n+3$ sites, i.e., on X to the right of a Pt^{IV} site. Positive kinks (K^+), however, prefer $4n+1$ sites, e.g., on X to the left of a Pt^{IV} site. This corresponds to the more delocalized case in the $t_0=0$ limit.[40] When two neutral or charged kinks are placed on a chain with $N=4n$, either nearby or separated, one of the kinks locates itself at a $4n-1$ site while the other locates at a $4n+1$ site. (This agrees with the above, since the phase of the ground state is reversed from the point of view of the second kink.) Note that such a selectivity for sites is much more diverse here than in half filled one-band models.

2. Energetics. Total energy (electron plus lattice) per site $E = E_T/N$, relative to the undistorted phase, is an indicator of the CDW strength. Thus, for the localized (strong CDW) case the energy is lowest while for delocalized (weak CDW) case the energy is highest. PtBr represents an intermediate regime. For defects, one needs to compare the difference in total energy with that of the ground state. Since the defects are localized this should be independent of system size for sufficiently large systems. For all three cases, positive excitations have lower energy with respect to the uniform case while neutral and negative excitations have higher energy ($E^+ < E^u < E^0 < E^-$). This is because, in our two-band formalism, we defined the gap to be not around zero energy, but rather near $+e_0$. To compare energy costs of creating defects, we need to calculate the energy with respect to adding an electron at the center of the gap: i.e., we must explicitly include the chemical potential. We define the creation energy to be

$$E^{\rm cr} = E_T^d - \mu N_e^d - E_T^u + \mu N_e^u \ , \tag{18}$$

where u, d refer to uniform and defect states, $\mu = (e^v + e^c)/2$, and $e^{v,c}$ is the single-particle energy of the level at the top of the valence band (bottom of conduction band). N_e denotes the total number of electrons. The creation energies of various defects for the PtX materials are listed in Table III. For PtCl the hierarchy of the creation energies is

$$E^{\rm cr}_{2P+} > E^{\rm cr}_{2P-} > E^{\rm cr}_{B^0} > E^{\rm cr}_{2K^0} > E^{\rm cr}_{B^{2-}} > E^{\rm cr}_{2K-} > E^{\rm cr}_{B^{2+}} > E^{\rm cr}_{2K+} > 0,$$

where the uniform ground state has zero creation energy by definition. This hierarchy is modified for PtBr as

$$E^{\rm cr}_{2P+} > E^{\rm cr}_{2P-} > E^{\rm cr}_{2K-} > E^{\rm cr}_{B^{2-}} > E^{\rm cr}_{B^0} > E^{\rm cr}_{2K^0} > E^{\rm cr}_{B^{2+}} > E^{\rm cr}_{2K+} > 0.$$

PtI is similar to PtBr except that $E^{\rm cr}_{B^{2-}} > 2E^{\rm cr}_{K-}$. Note that the energies of the positive and negative versions of the same defect are not equal, even in the absence of e-e correlations. This is a manifestation of the electron-hole asymmetry inherent in the two-band model. The polarons are the highest-energy defects in all cases. While the relative ordering of the bipolarons and kinks depends on charge, for a given pair of like charges, two kinks are, in general, favored over the corresponding bipolaron. We

TABLE III. Creation energy of the polaron (P), bipolaron (B), and kink (K) (e denotes electron; n denotes neutral; h denotes hole) above the charge neutral ground state in units of half the uniform electronic energy gap for the PtX parameters of Table II. For $e_0 \to \infty$ the one-band model (Ref. 9) predicts $E^{\rm cr}_{2P}/E^{\rm cr}_B = 1.2$ and $E^{\rm cr}_{2K}/E^{\rm cr}_B = 1.0$. For the P and K, the energy per defect for the case of two nearby defects (separation less than the width) is also listed. For separation greater than twice the soliton width, the energy was the same as the isolated defect, to numerical accuracy. The energies not listed could not be determined, as those nearby defects were not even metastable against the bipolaron.

		P		$B/2$	K	
		Isolated	Nearby		Nearby	Isolated
PtCl	e	0.7398	0.7373	0.5601	0.5486	0.5493
	n			0.6218		0.5984
	h	0.8713	0.8728	0.5010		0.4392
PtBr	e	0.8272	0.8267	0.6246	0.6246	0.6315
	n			0.6169		0.6124
	h	0.8808	0.8814	0.5299	0.5298	0.5214
PtI	e	0.8768	0.8775	0.6562		0.6555
	n			0.6317		0.6293
	h	0.8962	0.8975	0.5998		0.5965

have also compared the energies of the two nearby or separate kinks and polarons with that of a bipolaron. We note that (i) for all PtX

$$E^{cr}_{2P+,near} > E^{cr}_{2P+,sep} > E^{cr}_{B^{2+}} > E^{cr}_{2K+,near} k > E^{cr}_{2K+,sep},$$

(ii) for PtCl

$$E^{cr}_{2P-,sep} > E^{cr}_{2P-,near} > E^{cr}_{B^{2-}} > E^{cr}_{2K-,sep} > E^{cr}_{2K-,near},$$

and (iii) the electron defects for PtBr and PtI behave similar to PtCl defects in (ii) above except that for PtBr

$$E^{cr}_{2K-,sep} > E^{cr}_{2K-,near} = E^{cr}_{B^{2-}}$$

and for PtI

$$E^{cr}_{P-,near} > E^{cr}_{P-,sep}.$$

These trends in Table III can be understood as follows. In the localized limit ($t_0 \to 0$; PtCl is closest to this limit) the creation energies of various defects are

$$E^{cr}_{2K^0} = E^{cr}_{2P-} = E^{cr}_{2P+} = E^{cr}_{1.5B^{2-}} = E^{cr}_{1.2B^0}$$

and

$$E^{cr}_{2K-} = E^{cr}_{2K+} = E^{cr}_{B^{2-}} = E^{cr}_{B^{2+}},$$

which explains the values for PtCl. In the delocalized limit the difference in the elastic energy of various excitations is inconsequential. It only depends on the filling of electronic levels. In this regime $E^{cr}_{2K^0}=E^{cr}_{B^0}$ and $E^{cr}_{2K-}=E^{cr}_{2K+}=E^{cr}_{B^{2-}}=E^{cr}_{B^{2+}}$. Kink levels are closer to midgap while the polaron levels are closer to the band edges. Therefore, for kinks the elastic energy is more important than the electronic energy. The case is reversed for polarons. Thus $E^{cr}_{K-} > E^{cr}_{K+}$ while $E^{cr}_{P-} < E^{cr}_{P+}$. In general, hole defects are more delocalized. Since $E^{cr}_{B^0} > E^{cr}_{B^{2-}} > E^{cr}_{B^{2+}}$ and $E^{cr}_{K^0} > E^{cr}_{K-} > E^{cr}_{K+}$ for PtCl, while $E^{cr}_{B^{2-}} > E^{cr}_{B^0} > E^{cr}_{B^{2+}}$ and $E^{cr}_{K-} > E^{cr}_{K^0} > E^{cr}_{K+}$ for PtBr and PtI, somewhere for a parameter set between PtCl and PtBr there is a crossover between the trends for neutral excitations.

3. Trends in intragap absorption. Next we examine the parameter dependence of the electron (P^-) and hole (P^+) polarons. A number of important observations can be made. First, for small Δ the polaron electronic spectrum with two intragap states is similar to that of the polaron in the SSH model of polyacetylene.[38,41] Second, increasing Δ sharply decreases the width of the polaron toward the valence trapped limit. In accord with results from the one-band model for large Δ,[9] there are also three intragap absorptions associated with the polaron. As discussed in detail below, the transitions from the lower gap state to the conduction band and from the M valence band to the upper gap state are similar in strength to the transition between the gap states and are an order of magnitude stronger than the absorption arising from transitions between the upper (lower) gap state and the conduction (valence) band, in sharp contrast to the small Δ absorption. Third, although increasing e_0 opens a gap between the low-energy predominantly X states and the higher-energy predominantly M states, it does not decouple them, as there is an extremely strong X-M absorption peak at higher energies. Fourth, defect absorptions are seen to the blue as well as to the red of the gap. Unlike the one-band model,[9] the two-band model has no electron-hole symmetry even in the absence of correlations. This is a manifestation of the $\frac{3}{4}$-filled band and is not observed in the $\frac{1}{2}$-filled AB model[28,42] or in the one-band version of this model.[9] For positively and negatively charged defects this is reflected in differences in both the locations of the localized intragap states and in differences in the associated optical absorptions. At fixed small Δ the polarons have little parameter dependence (for both $K_{MM}=0$ and $K_{MM} \to \infty$) and for larger Δ only a moderate parameter dependence is seen, as shown in Figs. 6 and 7. From this we deduce that Δ is the important quantity for the polarons. Further, at large Δ the parameter dependence is weaker for the electron polarons. This can possibly be understood by looking at the excess charge densities [see, e.g., Fig. 17(a)]. For the electron polaron, there is very little charge density on any M except the one at the defect center. For the hole polaron, there is a strong parameter dependence of the excess charge on the nearest and next-nearest neighbor M. The Δ dependence of the absorptions is shown in Fig. 8 for typical parameters and large and small K_{MM}.

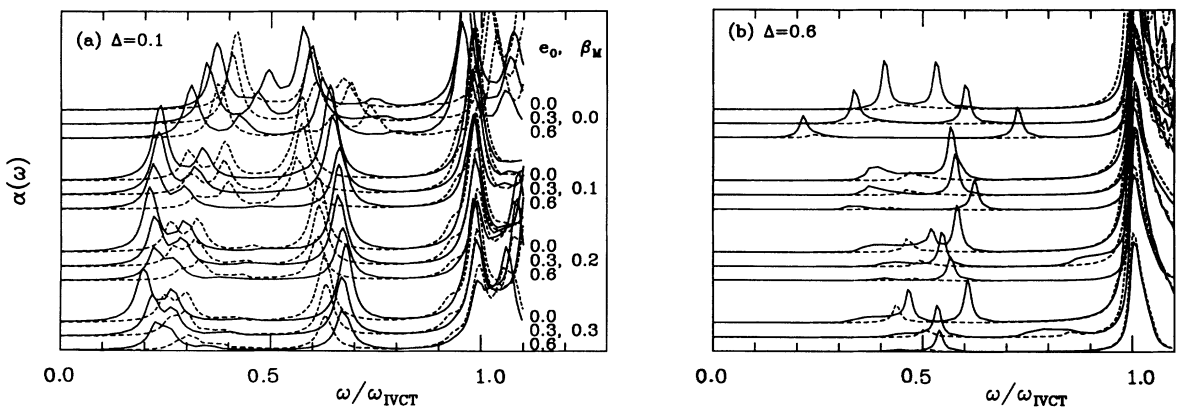

FIG. 6. Electron (dashed) and hole (solid) polaron optical absorption as function of e_0 and β_M at (a) $\Delta = 0.1$ and (b) $\Delta = 0.6$ for $K_{MM} = 0$. The structure above the IVCT for $\Delta = 0.1$ is due to discreteness effects (level spacing in band).

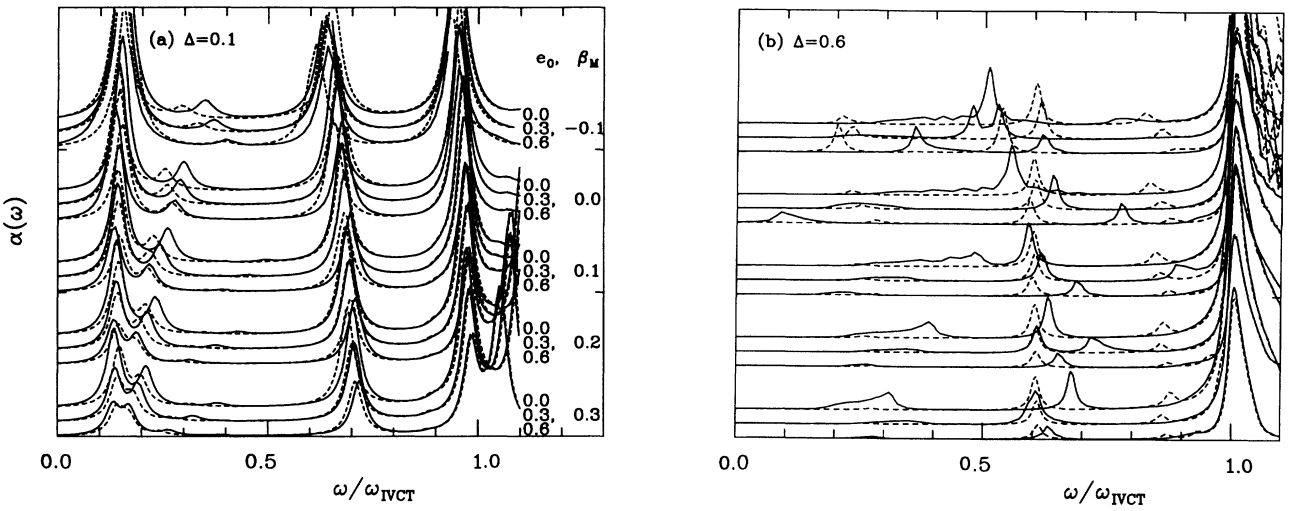

FIG. 7. Same as Fig. 6 but $K_{MM} \rightarrow \infty$.

As just noted, the Δ dependence is strong, as is the K_{MM} dependence at large Δ. However, at small Δ, the value of K_{MM} is unimportant for the defect absorptions. The trends with K_{MM} for a typical parameter set are shown for polarons, bipolarons, and kinks, with parameters corresponding to both small and large distortion, in Figs. 9, 10, and 11, respectively. Trends for the electron and hole bipolarons as well as the neutral and charged kinks are discussed in more detail below. We find, as might be expected, bipolarons are narrower and deeper than the corresponding polarons, and have associated localized electronic states occurring deeper in the gap. As can be seen from Table III, the polaron is less stable than a charged and neutral kink pair, while the charged kink pair is marginally more stable than a bipolaron and much more stable than a pair of charged polarons. In the valence-trapped limit (large β) the bipolaron is virtually indistinguishable from the kink pair. The relative stability of the kink and polaron defects increases with increasing β, but decreases with increasing e_0. However as we discuss elsewhere[9,30] the relative stability of polarons with respect to kinks or bipolarons is sensitive to both U and V. In particular, V_{MM} favors excitons.

B. PtCl, PtBr, and PtI

1. *Electronic energy levels*

The energy levels are shown in Fig. 12 for PtCl, PtBr, and PtI. For the uniform ground state (U) there are four bands. The lower two bands correspond to X majority bands and are filled. The upper two bands belong to the metal (Pt). The top M band is empty; the lower M band is filled. The gap between these two bands is referred to as the IVCT (intervalence charge transfer) gap. Overall the system is $\frac{3}{4}$ filled in the ground state. Note that in Eq. (2a) we defined the zero of energy to be in between the upper X band and the lower M band. However, in Fig. 12 we have shown the zero of energy at the top of the metal valence band to facilitate comparison of the energy of intragap levels (due to nonlinear excitations discussed below) with respect to the IVCT. The trend to the more delocalized system as X varies from Cl→I can be easily seen from the figure. In PtCl the bands are narrow with wide gaps since PtCl is a strongly localized system. On the other hand in PtI the bands are quite wide with small gaps since PtI is a weakly localized system. PtBr is a moderately localized system and therefore both the

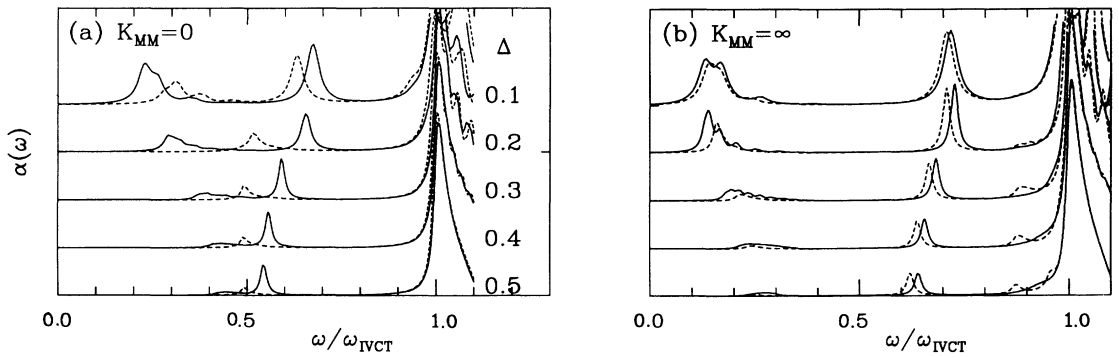

FIG. 8. Electron (dashed) and hole (solid) polaron optical absorption as a function of Δ for $e_0 = 0.6$ and $\beta_M = 0.3$; (a) $K_{MM} = 0$ and (b) $K_{MM} \rightarrow \infty$.

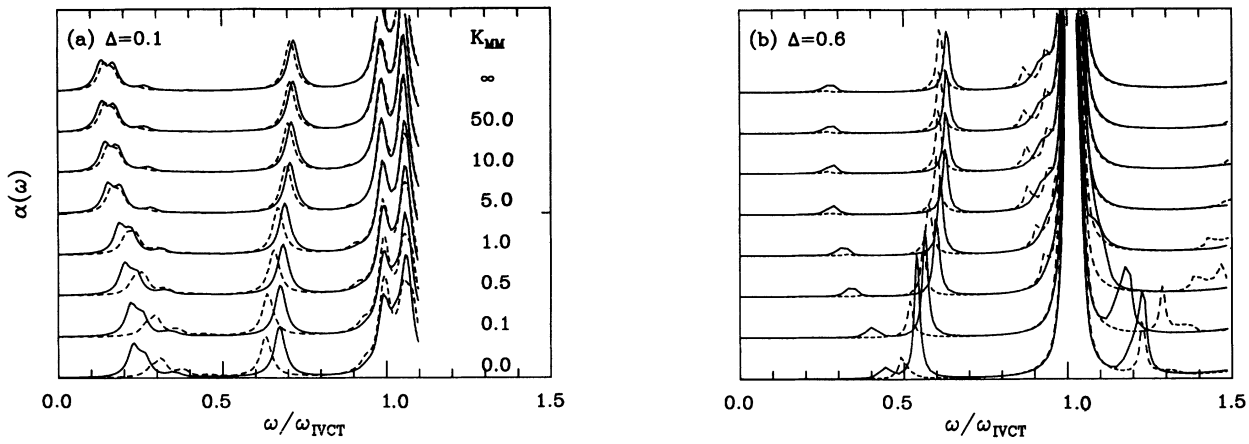

FIG. 9. K_{MM} dependence of the optical absorption of the electron (dashed) and hole (solid) polarons for $e_0 = 0.6$ and $\beta_M = 0.3 = -2\beta_X$ at (a) $\Delta = 0.1$ and (b) $\Delta = 0.6$.

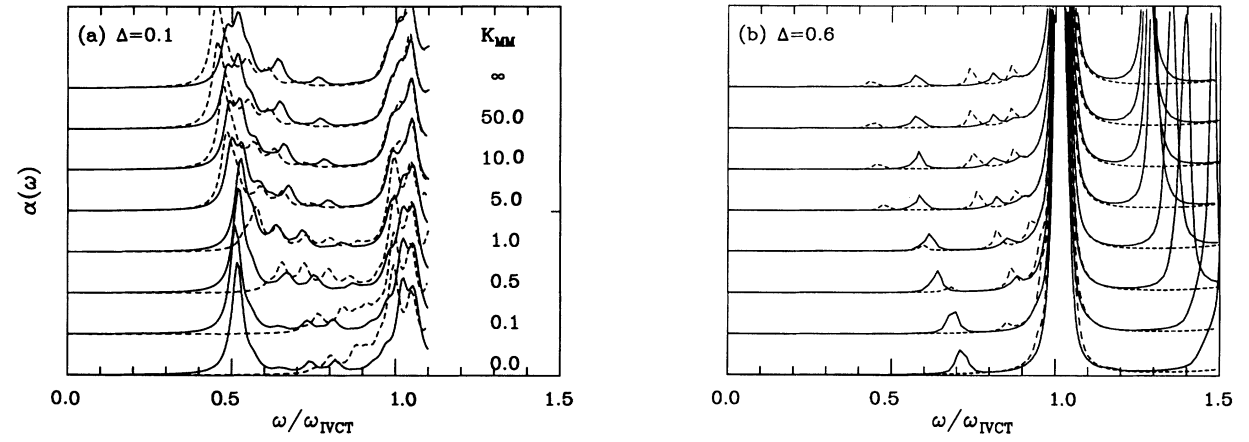

FIG. 10. K_{MM} dependence of the optical absorption of the electron (dashed) and hole (solid) bipolarons for $e_0 = 0.6$ and $\beta_M = 0.3 = -2\beta_X$ at $\Delta = 0.6$.

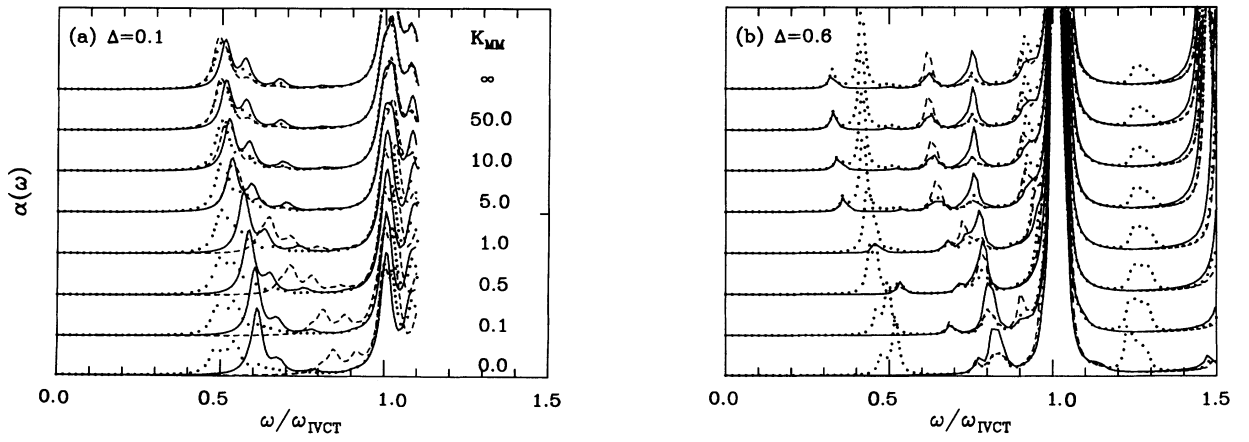

FIG. 11. K_{MM} dependence of the optical absorption of the electron (dashed), neutral (dotted), and hole (solid) kinks for $e_0 = 0.6$ and $\beta_M = 0.3 = -2\beta_X$ at $\Delta = 0.6$.

band widths and gaps have intermediate values. PtBr, however, is closer to PtI in terms of the localized or delocalized crossover, characterized by lattice pinning, etc. Our PtX parameters do not show the change in ordering of the majority bands discussed in Sec. III A.

When electrons are added to (or removed from) an MX chain via doping, depending on the system and chain length, different nonlinear excitations are formed. These introduce localized levels in the IVCT gap. In addition, the continuum states are phase shifted. For an electron polaron (P^-) in PtCl, Fig. 12(a) shows two localized levels in the Peierls (IVCT) gap almost symmetrically placed. For a hole polaron (P^+) these intragap levels are shifted up in energy. Additionally, a weakly localized level appears close to the bottom of the empty Pt band.[43] The asymmetric location of the intragap levels is clearly a manifestation of the two-band nature of the model. Furthermore, the disparity of the P^+ and P^- intragap features indicates that there is no charge-conjugation symmetry in this model, which is again related to the $\frac{3}{4}$-filled, two-band character of the model.[44] Note that similar localized levels are also present in the gap between the two X bands. However, these levels are filled regardless of the excitation under consideration. As the system becomes moderately localized [PtBr, Fig. 12(b)] the asymmetry in polaronic intragap features diminishes and so does the difference between the energy levels of P^+ and P^-. In the weakly localized case [PtI, Fig. 12(c)] the asymmetry is virtually nonexistent and the intragap levels of P^+ and P^- begin to resemble each other. If we discard the X bands, PtI electronic band structure appears quite similar to that of *trans*-polyacetylene. In fact PtI is even more delocalized than *trans*-$(CH)_x$.

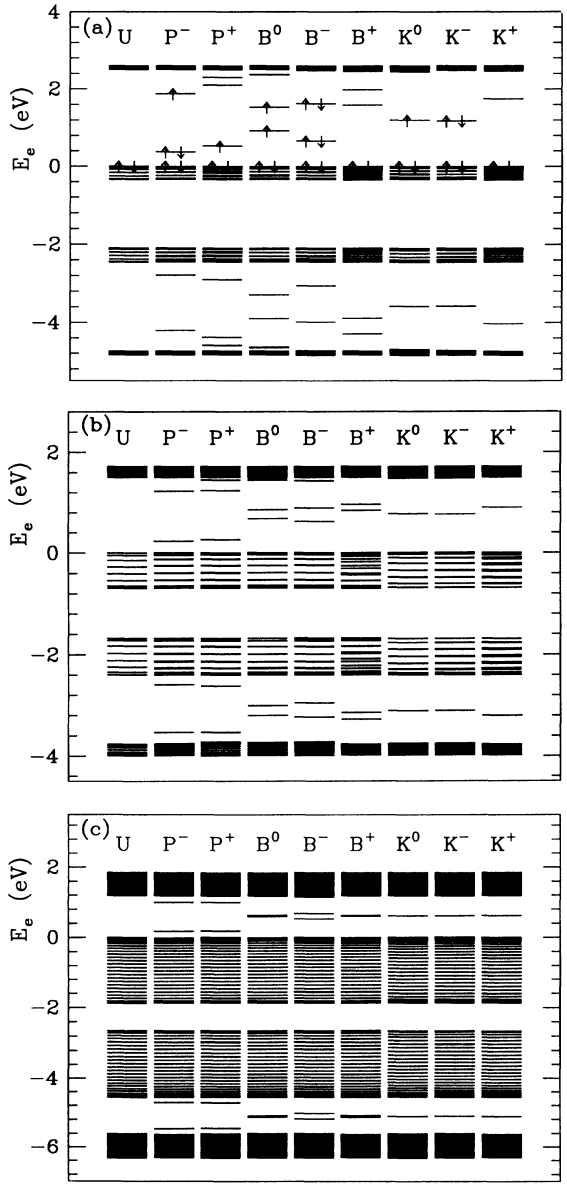

FIG. 12. Energy-level diagrams for uniform ground state (U) and various charged and neutral nonlinear excitations, namely kink solitons (K), polarons (P), and bipolarons (B) for (a) PtCl, (b) PtBr, and (c) PtI (parameters of Table II). For convenience the zero of energy is shown at the top of the metal (M) valence band instead of in the middle of metal valence and halide (X) conduction bands.

Paramagnetic polarons can combine to form bound diamagnetic entities called bipolarons. For a P^- the lower localized level is filled while the upper level has one electron. In B^{2-} both intragap levels are filled. For a P^+ the upper localized level is empty while the lower level has one electron in it. In a B^{2+}, however, both intragap levels are empty. The two intragap levels associated with a B^{2-} lie deeper in the Peierls gap as compared to the corresponding P^-. The same holds true for a B^{2+}. Nevertheless, both B^{2+} intragap levels are located in the upper half of the gap [Fig. 12(a)]. As the system becomes more delocalized the bipolaron levels fall deeper into the gap and the asymmetry between B^{2+} and B^{2-} diminishes significantly [Figs. 12(b)and 12(c)]. There is a third kind of bipolaron which is not accessible to doping but can be generated during photoexcitation. This neutral bipolaron (B^0) is usually called an exciton, though sometimes referred to as a "polarexciton." There are two intragap levels, each singly occupied, associated with a B^0. These are almost symmetrically located about midgap. In addition, there is a localized level close to the bottom of the M conduction band. Depending on the spin of the electrons in the localized levels, an exciton can be either in a singlet or a triplet spin state.[45] As the system becomes more delocalized, the B^0 intragap levels tend to fall deep into the gap whereas the level near the bottom of the M conduction band merges into this band.

A chain of length $4n+2$ intrinsically has a neutral kink soliton (K^0) present due to topological reasons (recall we are employing periodic-boundary conditions). There is an intragap level almost in the middle of the Peierls gap. This level has a single electron in it and thus a K^0 is paramagnetic. When a chain with a neutral kink is doped, diamagnetic charged kinks are created. This separation of spin and charge, familiar from the $\frac{1}{2}$-filled one-band model of polyacetylene, is, however, not as clean in the $\frac{3}{4}$-filled case, as discussed in more detail below. Similar to the K^0, the K^- also has a localized level near midgap, but in this case it is filled. A K^+ has an empty intra-

gap level which is located off-center towards the bottom of the M conduction band. Akin to polarons and bipolarons the asymmetry between K^+ and K^- is prominent in the strongly distorted case (PtCl), is reduced in PtBr and almost vanishes in the weakly distorted case (PtI). In fact, the intragap level for all three kind of kinks is at midgap for PtI; in this delocalized limit the kinks differ only in level filling.

2. *Density of states and wave functions*

Figure 13 depicts density of states and Fig. 14 the wave functions for a few representative cases. Specifically, Fig. 13(a) shows electronic density of states as a function of energy in the presence of an electron polaron in PtCl. Both M and X bands are quite narrow. In addition, two localized levels in the Peierls gap are clearly visible. Two levels in the gap between the X bands are also present. These peaks and the bands were Lorentzian broadened. Figure 14(a) shows an electronic wave function corresponding to the upper localized level of a hole polaron. Alternating energy levels have even and odd spatial symmetry. The level shown here has an odd symmetry. Note that this wave function has significant amplitude over 5 Pt_2Cl_2 units. The wave function for P^+ (not shown here) is slightly less extended.

Figure 13(b) shows electronic density of states in the presence of a hole bipolaron in PtBr. Note that the bands are wider than in PtCl. Two closely spaced localized levels associated with B^{2+} are present in the Peierls gap. These are located off-center as seen from the energy-level diagram [Figure 12(b)]. Similar localized levels are present in the gap between the X bands. Figure 14(b) depicts an electronic wave function associated with lower localized level of an electron bipolaron. This particular wave function is symmetric and has significant amplitude over 10 Pt_2Br_2 units.

Figure 13(c) depicts electronic density of states in the presence of a neutral kink soliton in PtI. Clearly the bands are very wide and the band edges appear to diverge with a square-root singularity. A localized level associated with the kink is present at the center of the Peierls gap (and a corresponding level in the gap between the X bands). Figure 14(c) shows the electronic wave function of the neutral kink intragap level and has odd symmetry. The wave function has significant amplitude over at least 20 Pt_2I_2 units. Thus, kinks, polarons, and bipolarons are extremely mobile on a PtI chain.

3. *Optical absorption*

The absolute optical absorption per unit cell (M_2X_2 unit) for the uniformly distorted ground state is depicted

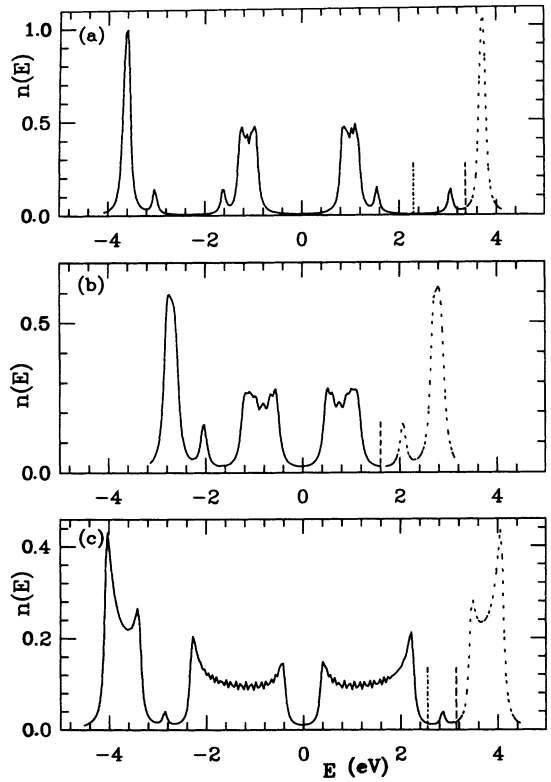

FIG. 13. Electronic density of states as a function of energy in the presence of (a) an electron polaron (P^-) in PtCl; (b) a hole bipolaron (B^{2+}) in PtBr; and (c) a neutral kink (K^0) in PtI. The vertical lines indicate the Fermi level for the two spins and the density of states for unoccupied levels is dashed. The localized levels in addition to four bands are clearly visible (see Fig. 12).

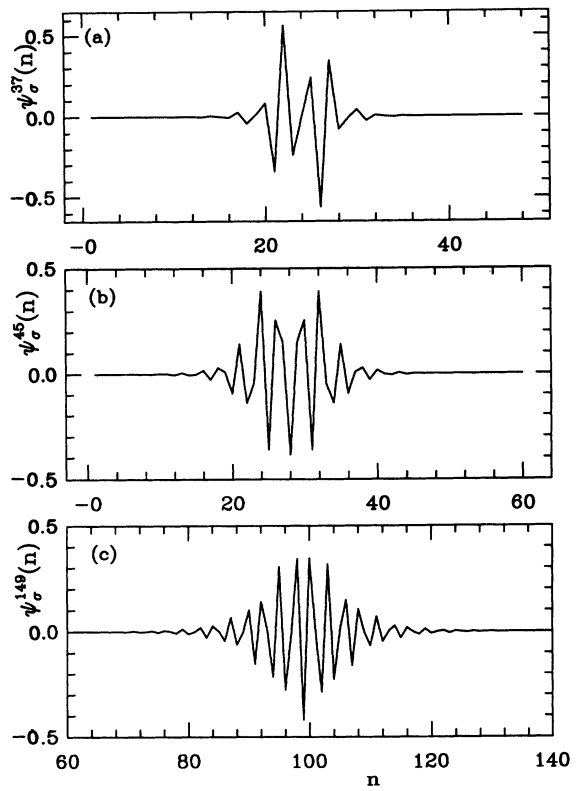

FIG. 14. Electronic wave functions corresponding to (a) the upper localized level of a hole polaron (P^+) on a PtCl chain; (b) the lower localized level of an electron bipolaron (B^{2-}) on a PtBr chain; and (c) the midgap localized level of a neutral kink soliton (K^0) on a PtI chain. Note that the wave functions have either even or odd symmetry.

in Fig. 15. The optical absorption was calculated from the golden rule; the spectra were Lorentzian smoothed to mimic the experimental spectra. However, no inhomogeneous broadening was included. There are two peaks associated with the ground state. The lower peak is due to the transitions across the IVCT (M-M transition). The high-energy peak is due to the transitions between the upper X band and the upper M band (M-X transition). The transition from the lower X band to the M conduction band has negligible oscillator strength. The existing experimental data does not include the M-X transition peak [although there is evidence for the M-X absorption near 5.5 eV in reflectivity data for PtCl (Ref. 20)]. In the strongly distorted system (PtCl) the M-X transition is quite strong while in the weakly distorted system (PtI) it is very weak. As usual the M-X transition in PtBr has intermediate oscillator strength. With increasing strength of CDW, both height and width of the IVCT peak decrease which is consistent with experimental data.

Figure 16 depicts absorptions due to various nonlinear excitations in the PtX materials, with the absorption due to the uniform ground state subtracted to enhance the defect contribution. In the localized limit with large K_{MM}, there are three distinct intragap features (the so-called A, B, and C peaks) for both electron and hole polarons. These can be readily understood in terms of transitions between localized gap states (Fig. 12), and between the gap states and the continuum (band) states. The low-energy intragap (C) peak arises from transitions between the M valence band and the lower polaron level for P^+, and from transitions between the upper polaron level and M conduction band for P^-. The mid-energy (A) peak, which is the strongest intragap absorption, arises from transition between the intragap polaron levels. The high-energy (B) peak results from transitions between the M valence band and the upper polaron level for P^+, and from transitions between the lower intragap level and M conduction band for P^- (and vice versa). There is a peak beyond the IVCT and just below the M-X peak. In addition, there are two peaks beyond the M-X peak. These peaks arise from transitions between the X bands and the localized polaron levels. As mentioned above in the strongly distorted case (PtCl), the A peak is the strongest intragap transition and there is significant asymmetry between electron and hole polaron absorptions. As the strength of electron-phonon coupling

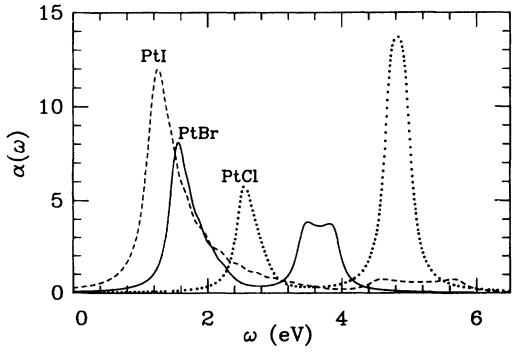

FIG. 15. Absolute optical absorptions per unit cell (M_2X_2 unit) for the PtX materials [PtCl (dotted), PtBr (solid), and PtI (dashed)] using the parameters of Table II. The spectra are Lorentzian broadened to match experimental spectra (Ref. 20). The trend to decreasing height and narrowing of the IVCT as the gap increases agrees with experiment.

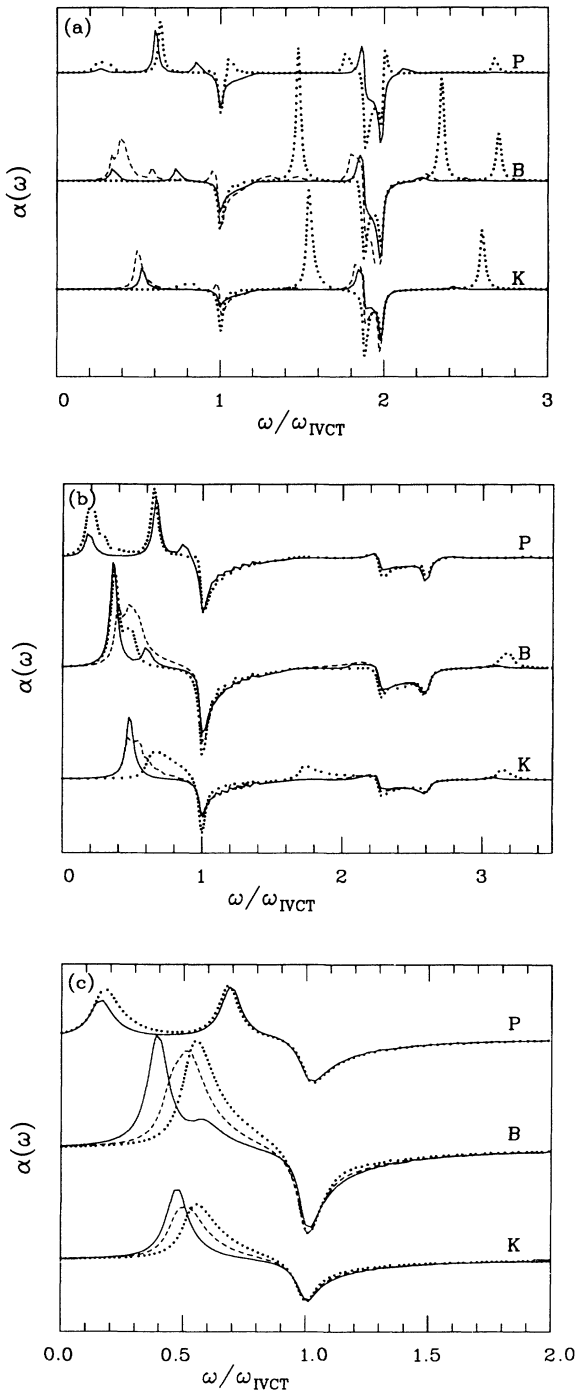

FIG. 16. Predicted optical absorption of P, B, and K defects for (a) PtCl, (b) PtBr, and (c) PtI, using the parameters of Table II. Difference spectra with the uniform absorption subtracted off are shown to enhance the structure due to defect absorptions. Electron defect curves are solid, hole defects are dotted, and neutral defects are dashed.

decreases, the B peak shifts towards higher energy and merges into the IVCT band for very weak e-ph coupling [PtI, Fig. 16(c)]. Furthermore, the C peak gains intensity until its oscillator strength roughly equals to that of the A peak, the peaks beyond the IVCT lose most of their oscillator strength, and the asymmetry between P^+ and P^- absorptions vanishes. The optical sum rule was checked to be satisfied within the numerical accuracy. Note that the M-X transition occurs around twice the IVCT in PtCl, between 2 and 3 times the IVCT in PtBr and around 4–5 times the IVCT in PtI [not shown in Fig. 16(c)].

The optical-absorption spectrum for charged bipolarons exhibits two main intragap features. Unlike polarons, charged bipolarons do not exhibit the midenergy intragap peak (the analog of the A peak) since the transition between localized states is forbidden due to the occupancy of the gap levels. For the neutral bipolaron, however, the low-energy intragap peak is a composite of four closely spaced peaks which arise from transitions between the gap states and the extended states.[45] The location of these peaks can be understood in terms of the level positions and occupations shown in Fig. 12. In the localized case there is one more intragap peak associated with the exciton just below the IVCT [see Fig. 16(a) for B^0]. This peak results from transitions into the localized level located just below the bottom of the M conduction band [compare Fig. 12(a)]. Note that akin to polarons the oscillator strength of the intragap absorptions associated with a hole bipolaron is much smaller compared to the oscillator strength of an electron bipolaron or an exciton in the localized case. On the other hand, a hole bipolaron has one very pronounced peak between the IVCT and twice the IVCT and two pronounced peaks beyond twice the IVCT. The oscillator strength for corresponding peaks for a B^{2-} or a B^0 is very small. As the system becomes delocalized the asymmetry between the B^{2+} and B^{2-} absorptions persists but gradually becomes less striking. Moreover, the two intragap peaks move closer and the peaks beyond the IVCT vanish. Indeed, for PtI the intragap levels for B^0 and B^{2+} are so close there appears to be only one broad intragap peak.

Kink optical absorptions show one intragap peak around the midgap corresponding to transitions between the localized soliton level and the continuum bands. The peak for K^+ is located closer to the IVCT which is consistent with the energy-level diagrams of Fig. 12. In general, the K^- peak is narrow and the K^+ peak is wide, K^0 being intermediate. Similar to a hole bipolaron, a hole soliton in the localized system has prominent peaks beyond the IVCT. However, unlike B^{2+}, there is only one peak beyond twice the IVCT which is related to the transition from the localized level between the X bands and the upper M band. The peak around $\frac{3}{2}$ the IVCT can be ascribed to transitions from the upper X band to the soliton level. Moreover, the bleaching at the IVCT and twice the IVCT are related to optical transitions arising from changes in the extended states due to the presence of a soliton. With decreasing strength of the CDW [Figs. 16(b) and 16(c)] the relative oscillator strength varies but the asymmetry between the electron and hole soliton absorptions persists. In addition, the peaks beyond the IVCT diminish in intensity.

4. *Excess spin or charge density and SDW or CDW*

Figure 17 depicts the atomic positions (lattice distortion pattern y_l, $y_{l+1} - y_l = \Delta_l$), and the excess (with respect to uniformly distorted ground state) spin and charge densities, for various nonlinear excitations. Figure 18 depicts the corresponding amplitude of the CDW

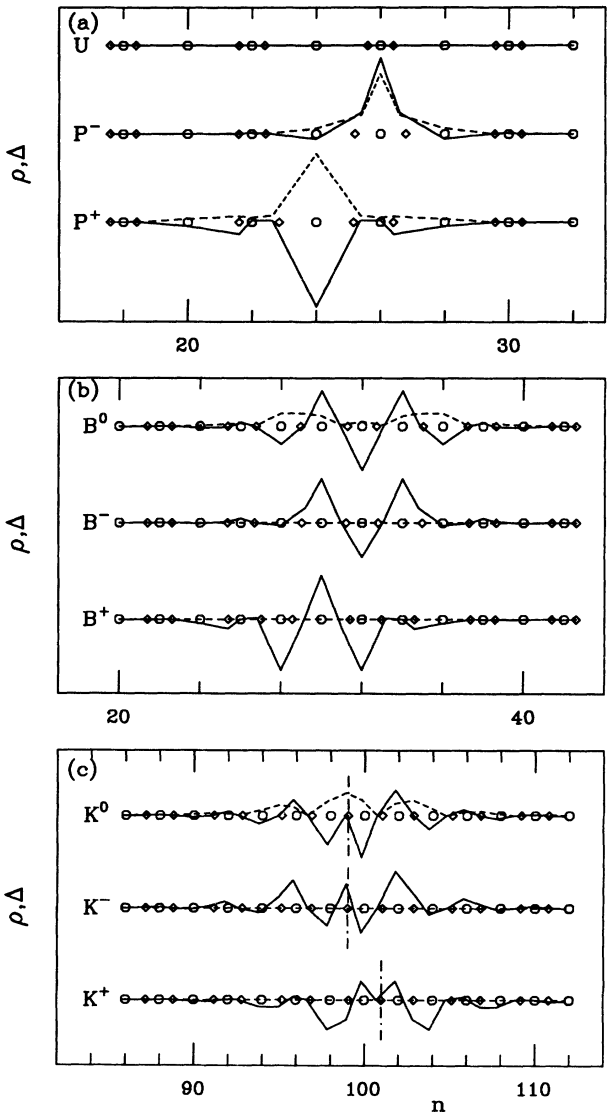

FIG. 17. (a) Excess charge (solid) and spin (dashed) density distributions (uniform chain values subtracted) of the P^+ and P^- defects for the strong CDW material PtCl (parameters of Table II). M (circle) and X (diamond) positions are indicated. For reference, the uniform ground state (U) is also shown. (b) Same as (a), but for bipolaron (B) defects in the intermediate strength CDW material PtBr. (c) Same as (a), but for kink (K) defects in the weak CDW material PtI. The phase of the uniform chain subtracted was shifted by 180° at the vertical dashed line.

and SDW order parameters. Since we are in a parameter space regime where $K_{MM} \to \infty$, the BOW amplitude is zero. For finite K_{MM}, a BOW distortion also appears. The shape of the BOW order parameter is essentially proportional to the derivative of the CDW order parameter. Figures 17(a) and 18(a) show results in the localized system, PtCl, for the uniformly distorted ground state as well as polarons. In the uniform ground state the halogen atoms move towards a metal (Pt) atom thereby creating alternating reduced ($Pt^{3-\delta}$, having long bonds on each side) and oxidized ($Pt^{3+\delta}$, having short bonds on either side) metal atoms. This charge disproportionation on the metal sublattice and the accompanying distortion of the X sublattice is what we refer to as the CDW. In the region of polarons this uniform distortion pattern is altered as shown in Fig. 17(a). A P^- favors an oxidized metal site while a P^+ favors a reduced metal site. The excess spin and charge densities indicate that a P^- extends over 2 Pt_2Cl_2 units while a P^+ extends over 3 Pt_2Cl_2 units. This asymmetry is clearly a two-band effect. The corresponding CDW, Fig. 18(a), reinforces this picture. The SDW amplitude is shown on both M and X sublattices. Although we do not show the results here, a B^{2-} extends over 3 Pt_2Cl_2 units while a B^{2+} or a B^0 extends over 4 Pt_2Cl_2 units. Similarly, neutral and charged solitons are localized on about 2 Pt_2Cl_2 units.

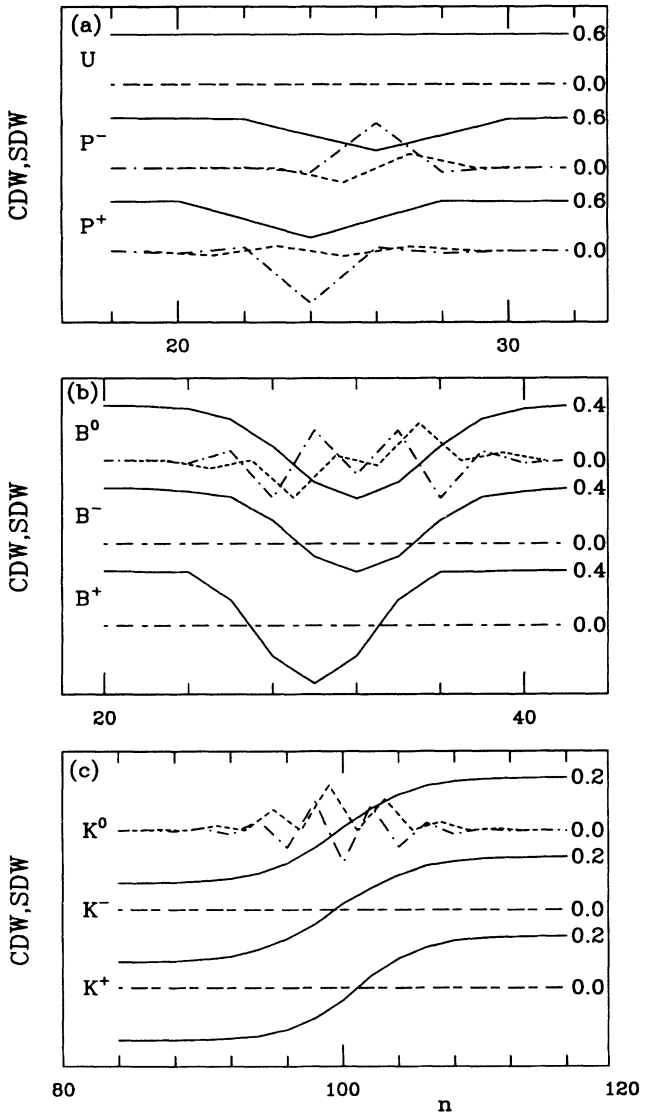

FIG. 18. CDW (solid), and SDW on both M (dot-dashed) and X (dashed) sublattices, in dimensionless units, corresponding to cases (a)–(c) of Fig. 17. The BOW is nonexistent for $K_{MM} \to \infty$ and varies essentially as the derivative of CDW for finite K_{MM}.

Figures 17(b) and 18(b) depict bipolarons in the more delocalized system, PtBr. Charged bipolarons are diamagnetic and thus do not exhibit excess spin density. The exciton, however, shows both excess charge and spin density owing to the unpaired electrons in the localized levels (though the integrated excess charge is, of course, zero). B^{2-} extends over 4 Pt_2Br_2 units whereas B^{2+} and B^0 extend over 5 Pt_2Br_2 units. Corresponding values for polarons and kink solitons (not shown here) are about the same. The CDW amplitudes exhibit bigger dips as compared to the polarons in this system. Since these excitations in PtBr are much more extended than in PtCl, the lattice pinning is quite reduced and they are much more mobile. The value of lattice pinning in PtCl is essentially infinite on a thermal scale, while in PtBr it is on the order of 10 K. From this perspective PtBr is closer to PtI than PtCl.

Figures 17(c) and 18(c) show results for kink solitons in the weakly localized system, PtI. The kink profiles connect the two uniform segments of the chain which are degenerate in energy, but with the sign of the CDW order parameter reversed (long and short bonds switched). K^- extends over 7 Pt_2I_2 units. As usual, K^0 and K^+ extend over more units. Corresponding polarons and bipolarons (not shown here) extend over as many as 21 Pt_2I_2 units. Consequently they are extremely mobile on the chain. The distortion patterns for the kinks are somewhat asymmetric since they are not quite at the minimum energy position, though converged to numerical accuracy, since symmetry was not enforced and lattice pinning effects are negligible. Akin to the bipolarons, charged kinks are spinless and only the neutral kink exhibits an excess spin density. (Note, however, that finite U restores spin density to the charged kinks, as discussed in paper II.) As expected from a $\frac{3}{4}$-filled, two-band model, both neutral and charged kinks exhibit excess charge density. In a $\frac{3}{4}$-filled, one-band model, one expects excess charge in units of $\frac{1}{2}$ an electron.[46] However, due to the two-bandedness,[28] the integrated excess charge is, in general, irrational. For the PtI case shown in Fig. 17(c), we find $-0.67e$, $0.65e$, and $0.34e$ excess charge for the K^-, K^+, and K^0, respectively.

C. Photoexcitation

Some defect states are inaccessible via impurity doping, e.g., the neutral bipolaron ("polarexciton"), but may be obtained during photoexcitation. This evolution should be compared with that of the singly photoexcited state in polyyne.[47] Mishima and Nasu[31] found that in a

one-band Hubbard model including V_{MM}, although two kinks are more stable, photoexcitation was predicted in HF to generate the excited polaron configuration. We note that, unlike *trans*-$(CH)_x$, which only shows a BOW and a single time scale governs the molecular dynamics, the PtX systems exhibit two time scales: the slower corresponds to the BOW, while the faster to the CDW distortion. We also note that a similar situation occurs in the cuprate HTSC. There, as in the NiX materials, relaxation upon doping into the SDW ground state of the stoichiometric materials occurs on different time scales for the spin and the lattice distortion order parameters. We anticipate that photoexcitation measurements in MX materials, and similarly in HTSC materials, should be able to resolve these two competing time scales experimentally.

Previous photoexcitation studies in polyacetylene and other conducting polymers have provided important insights, e.g., the role of kink solitons and the presence of breathers[48] (charge-neutral, spatially-localized, time-periodic, intrinsically dynamic, persistent, nonlinear lattice excitations), which can account for anomalies in the near band-edge photoabsorption spectrum in *trans*-polyacetylene and other conjugated polymers.[49] The evolution of a photoexcited system is dependent on a number of factors. First, the electronic occupancies of the photoexcited state place restrictions on the type of excitation that can be produced. A second constraint is introduced by the energy of these excitations relative to the energy added in photoexcitation. Thus by varying the pumping frequency of a photoexcitation one may, at least in principle, explore a number of different photoexcitation pathways. Third, because a nonlinear excitation is a strongly coherent, localized state it may predispose the evolution of the system to coherency, rather than incoherency. Finally, impurities and lattice discreteness affect the photodecay channel.

Photoexcitation is simulated numerically, as described in Appendix A, by manually removing an electron from an occupied state and instantaneously placing it in an unoccupied state. The system is subsequently allowed to evolve adiabatically according to Eq. (A9), with no further changes in electronic occupations. We simulated several photoexcitation experiments, which are expected to be significant experimentally: (i) photoexcitation of the ground state, and (ii) photoexcitation of an electron polaron.[50] We parameterized Hamiltonian Eq. (1) according to PtCl and the metal atoms were fixed at their lattice sites (i.e., $K_{MM} \to \infty$).

Figure 19 shows the evolution of PtCl after a single electron is photoexcited across the energy gap from the highest occupied level to the lowest unoccupied level, with the addition of the gap energy to the system. (Scaling as in Table III, we have added 2.0 energy units.) As is clear from Fig. 19(a), the system evolves to a separating kink-antikink pair. The electronic occupancies of the excited state necessitates that both of these kinks are neutral. Table III shows the creation energy of a static $K^0\overline{K^0}$ pair is 0.598 of the gap energy (1.196 energy units). Clearly while some of the remaining energy goes into both the kinetic energy of the kink and into acoustic phonon energy, Fig. 19 shows that a significant amount of energy is localized in the form of a small amplitude localized breather between the kinks. Similar breathers, temporally and spatially coherent bound states of optical phonons, have been seen in photoexcitation simulations in, e.g., polyacetylene.[48,49] Figure 19(b) shows the time evolution of characteristic gap states of a K^0 pair. Within a phonon period (~150 fs) two continuum states are pulled into the gap and then merge into one degenerate midgap state indicating that the initial electron-hole pair quickly evolves into a kink-antikink pair. At the same time a breather level oscillates about the conduction-band edge into the gap and persists with a time period larger than the phonon period.

To contrast the above simulation, we photoexcited an electron between the two gap states of an electron polaron, with the addition of approximately 1.205 of energy to the system. Minus the static electron polaron creation energy of 0.740 this would give the system 0.465 of energy above the undistorted state. Contrary to expectation, Figure 20(a) shows that the photoexcited electron does not evolve into a K^-K^0 pair even though there is more

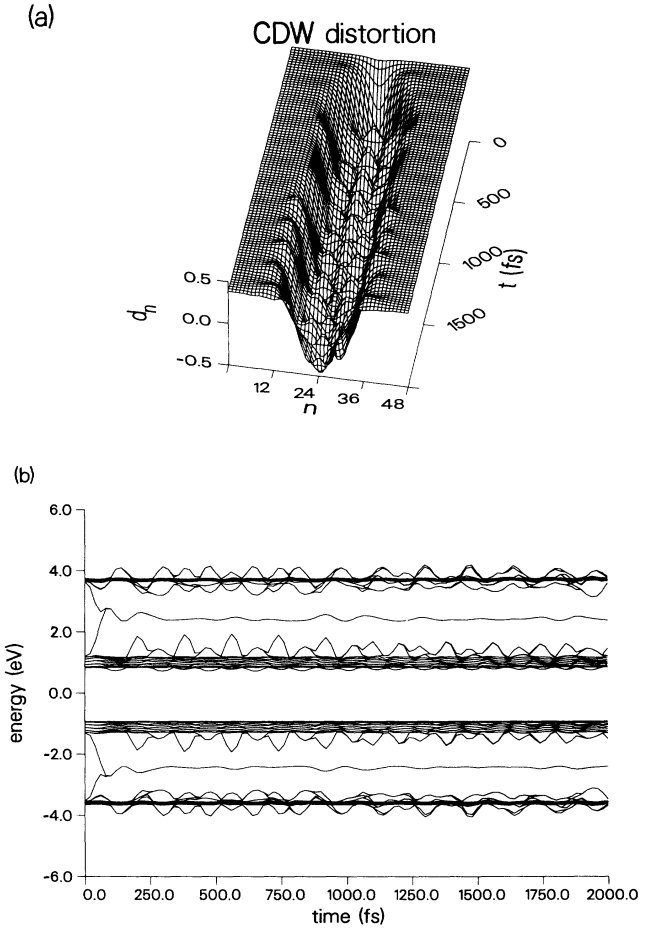

FIG. 19. Dynamics of photoexcitation: (a) CDW distortion as a function of time in units of 10^{-15} s and (b) energy levels as a function of time for photoexcitation of the ground state; for the PtCl parameters of Table II. Note the breather structure between the $K^0\overline{K^0}$ pair.

than sufficient energy to create the K^-K^0 pair (0.549 for K^- and 0.598 for K^0). Instead the excited polaron retains its identity and a substantial fraction of the input energy goes into the formation of breathers. Figure 20(b) shows the time evolution of corresponding intragap electronic levels. There is more than one breather present, which is consistent with the variation of breather amplitude in Fig. 20(a). In the uniform case discussed above, the $K^0\overline{K^0}$ pair separates initially but stops separating after about two phonon periods. On the other hand, the P^- is unable to break into a K^-K^0 pair. These observations indicate that the lattice pinning energy is very large in PtCl. However, in the case of PtBr, we find that[51] the corresponding kink pair and P^- separate rather than remain confined due to a small lattice pinning energy (about 10 K).

D. Comparison with experiment

In this subsection we compare some of our theoretical predictions with the available experimental data. Note that the majority of experimental data exists for localized systems. In the case of delocalized systems a clear distinction between A, B, and C peaks ceases to exist (see, e.g., Fig. 8).

Haruki and Kurita[16,22] have experimentally investigated the long-time evolution of photoexcited PtCl. Because the short-lived photoexcitation products will already have decayed this may be considered as a photodoping experiment.[52] They observed two high-energy absorptions (A and B peaks). A third (C) peak was recently observed in infrared absorption experiments on PtCl.[53] These results have been explained in terms of polaron formation. Analysis of resonance Raman data further resolves the A and B peaks into separate absorptions for the electron and hole polarons, and a bipolaron peak.[23,54] The locations of the experimentally observed intragap absorptions are in good agreement with the theoretical predictions, as can be seen from Figs. 21 and 16(a), and Table IV. The latter also provides the predicted absorption maxima for various kink and bipolaron defects. We stress that there are no free parameters used in this fit. Still, the theoretical values must be interpreted with a few caveats. First, the location of the C peak cannot be given correctly in this purely e-ph coupled model. Second, as discussed in paper II, e-e interactions affect the locations of the A, B, and C peaks, and the band-structure calculations indicate $U \gtrsim 0.5t_0$. Finally, the long-range Madelung terms (not included here) are also expected to affect peak positions.[34]

Though the short-time evolution of photoexcited PtCl is under investigation,[55] to date the only conclusive results are that the long-time photodecay products are polarons, as stated above. However, our preliminary results on photoexcitation across the gap (Fig. 19) predict that the favored photodecay channel should be a $K^0\overline{K^0}$ pair, though this scenario is likely to change when we include the on-site and nearest-neighbor Coulomb interactions (U_M, U_X, V_{MX}) in our dynamics simulations. Since photodecay channels sensitively depend on, among other factors, impurities and pinning centers, we do not find the current disagreement worrisome.

We are also in the process of calculating infrared and Raman frequencies.[56] The present parameter set for PtCl gives values of infrared and Raman frequencies which are about 20% below the experimental values.[24] We are trying to improve the present parameter set to remove this discrepancy by incorporating results from refined *ab initio* quantum chemistry[27] and band-structure calculations.[26] On the other hand the parameter set for PtBr predicts[56] values which are in excellent agreement with the experimental frequencies, as is evident from Table V.

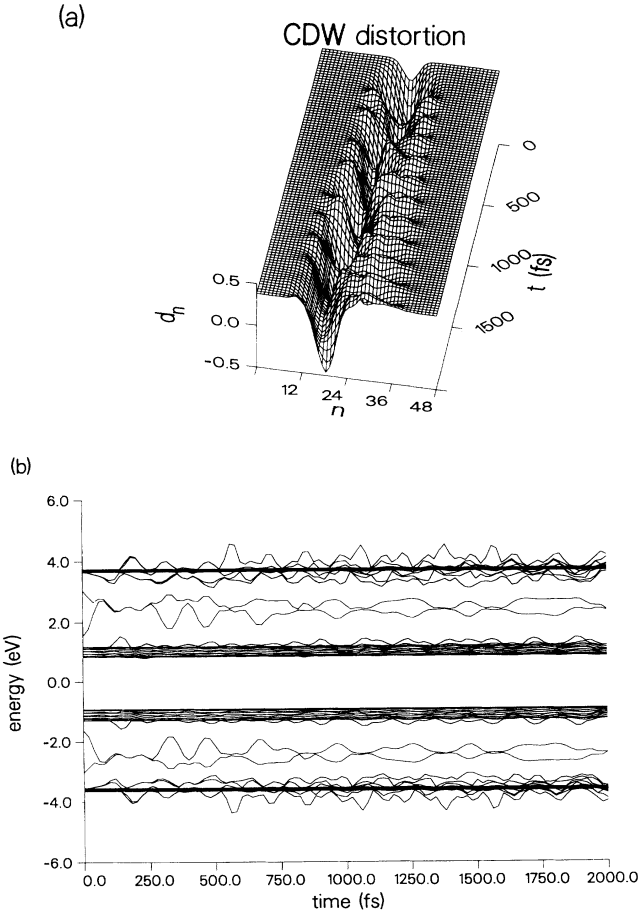

FIG. 20. Same as Fig. 19, but for an electron polaron.

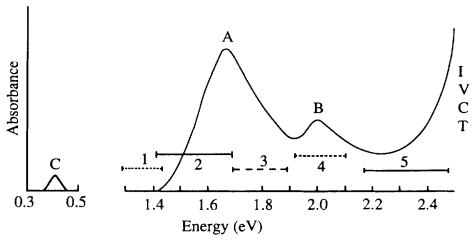

FIG. 21. The experimentally observed intragap absorption for PtCl (Ref. 54). Note how well it agrees with the predicted polaron spectra, Fig. 16(a).

TABLE IV. The energies of the maxima of the high-, medium-, and low-energy intragap absorptions relative to the IVCT band absorption energy. The experimental values are for PtCl (Refs. 16, 22, and 53) and the model values are from Fig. 16(a).

Expt.	P^-	P^+	B^{2-}	B^{2+}	K^-	K^0	K^+
0.84 (B peak)	0.86	0.94	0.74	0.78		0.99	0.82
0.70 (A peak)	0.60	0.64			0.52	0.48	
0.17 (C peak)	0.22	0.28	0.36				

Besides the single-crystal Raman, infrared, and optical-absorption mentioned above, magnetic susceptibilities[57] and ESR spectra,[16,17] of various MX and MMX materials have also been measured, though to date there is unfortunately no *single* MX chain material for which *all* this data exists. Even for PtCl the full intragap absorption spectrum has not been measured, partly due to the difficulty of spanning the spectral region between the A and C peaks, though this is currently being attempted.[58] There is some preliminary evidence of an additional peak near midgap, which could be fit by our predicted peak locations for the bipolarons or kinks. Existing data appears to be consistent with a model which includes some trapped polarons and some bipolarons which dissociate into polarons with temperature.[59] Finally, we comment that we do not expect real material effects (impurities, chain ends, grain boundaries, etc.) to significantly alter interpretation based on ideal chains. For instance, preliminary investigations of a weak trapping center (modeled as a screened point charge off the chain) indicate smooth shifts of predicted behavior for isolated impurities, as shown in Fig. 22. However, mixed metal systems may show interesting behavior, as discussed below.

V. DISCUSSION AND CONCLUSIONS

We have presented a comprehensive study of disproportionation (charge-density-wave) ground states and self-trapped excitations (solitons, polarons, bipolarons) in a $\frac{3}{4}$-filled, two-band, one-dimensional model Hamiltonian, which we believe captures the essential physics of individual chains of halogen-bridged transition metal (MX) complexes with weak electron-electron correlations, where interactions are dominated by intrasite electron-phonon interactions, driving the CDW ground states. While weak CDW and BOW situations have been extensively studied in simpler models (typically one band) and for other quasi-1D materials [e.g., a commensurate CDW in $(CH)_x$, or incommensurate in KCP], the MX chains provide the opportunity to tune quite continuously from weak (e.g., PtI) to intermediate (e.g., PtBr) to very strong (e.g., PtCl) CDW's. In this regard PtCl is distinctive because the discrete lattice effects are very influential — the CDW coherence length is of the order of the chain lattice constant. Thus, polaronic excitations are very strongly trapped on the lattice and photoexcitation and decay channels are dominated by this effect. PtBr already lies outside the strongly trapped limit and PtI completely so. However, the lattice pinning energies for polarons in PtBr are in an interesting regime experimentally, namely 10–100 K, which is indeed where various temperature sensitivities have been observed.

To give an interpretive framework for this broad range of materials, we have focused in this paper on *representative* parameter sets spanning the weak to strong CDW cases. In this way we hope to have provided a systematic summary of trends (reference resource) to guide future additions to the rapidly expanding experimental data base. We have focused on displacement patterns and optical-absorption signatures of ground states and self-localized excitations—solitons, polarons, and bipolarons. We have pointed to specific features of a $\frac{3}{4}$-filled two-band model including the possibility of long-period (superlattice) ground states, and local electronic levels associated with self-localized excitations which are located both in

TABLE V. Calculated (Ref. 56) Raman and upper (U) and lower (L) ir frequencies compared to the experimental values (Refs. 22 and 24) for PtBr.

	ω_{ir}^L (cm^{-1})	ω_R (cm^{-1})	ω_{ir}^U (cm^{-1})
Expt.		166	240
Theory	140[a]	167	240

[a]For K_{MM}=0.7.

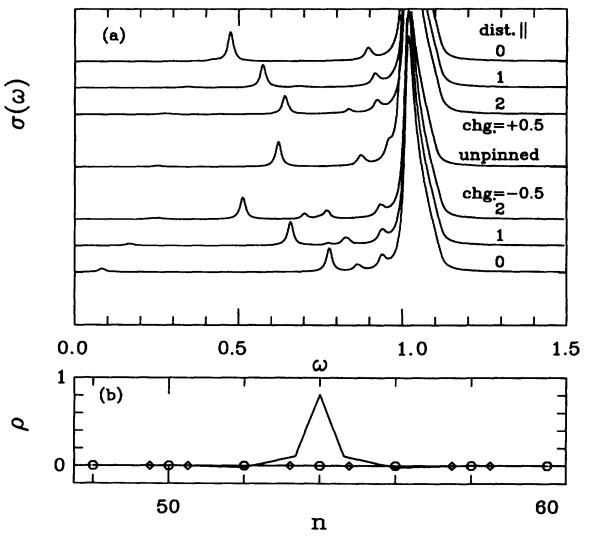

FIG. 22. (a) Pinning dependence of the optical absorption of the electron polaron for $t_0 = 0.5$, $\alpha = 0.5$, $K = 1$, $K_{MM} \to \infty$, $e_0 = 0.6$, $\beta_M = 0.3$, $\beta_X = -0.15$. The ICVT is scaled to 1. The difference in shifts with location of the pinning center relative to the unpinned defect center can be understood in terms of the excess charge density (b).

the semiconducting gap around the Fermi level ("intragap states") and outside the electronic bands ("ultragap states"). Furthermore, the two-band situation exhibits distinct electron-hole asymmetry, further distinguishing it from the $\frac{1}{2}$-filled, one-band model of electron-phonon coupling used, for example, to model $(CH)_x$. Some of these differences can be incorporated by, e.g., nonlinear electron-phonon coupling. However, we believe that the two-band model proposed here is most natural and fundamental.

Although we have not explicitly included the effects of Hubbard interaction for the results reported here, we do not anticipate our results to be altered significantly from a qualitative point of view for a small value of Hubbard U. Nevertheless, quantitative results, e.g., the energetics of bipolaron formation, would be changed somewhat. The parameters used here do include the effect of Hubbard U in an "effective $U=0$ HF" sense, since they are adjusted to match the real band structure with real e-e correlations. A systematic study of the effects of U in MX systems will be reported in paper II. We are also investigating the effects of including long-range electron-electron interactions representing Madelung fields, which are important in the strongly charge-disproportionated cases (e.g., PtCl), and for discussions of exciton formation.[34]

We emphasize that the two-band, $\frac{3}{4}$-filled model with competing electron-electron and electron-phonon interactions is fundamentally relevant to other novel electronic materials — e.g., cuprate and bismuthate high-temperature superconductors — when extensions to 2D and 3D are included. The bismuthates and cuprates have strongly charge-disproportionated and antiferromagnetic (dimerized SDW) reference phases, respectively. The SDW-type phases are indeed found in MX compounds when electron-electron interactions dominate, as discussed for NiBr and NiCl parameters in paper II. Understanding the nature of self-localized excitations and their pairing tendencies, as one follows the melting of CDW or SDW phases with temperature, pressure or doping, is a central issue, which may be illuminated by the systematic study available in the tunable MX or mixed-halide MX classes. Thus, for example, long-period superlattice phases and spin-Peierls phases (where spin order and lattice distortion occur simultaneously) are found theoretically and suggested in real MX and HTSC materials.

Though we have attempted here to give an overview of the basic behavior of electron-phonon interaction dominated MX chains, there are many interesting aspects of these materials upon which we did not touch. For instance, preliminary studies of mixed-halide systems, which we model as segments of one MX material (e.g., PtBr) in a chain of a second (e.g., PtCl), indicate that subsequent to doping or photoexcitation the electron and hole defects preferentially locate on differing chain segments (i.e., holes in the Cl segment, electrons in the Br segment), due to the polarization of the MX_2 unit at the interface and the interpenetration of CDW's. In other words, the mixed-halide chain acts as a photovoltaic device (in analogy with the usual semiconductor p-n junctions) and can possibly be used in, e.g., solar cell applications. In addition, the electronic and spectroscopic properties of MX crystals depend very sensitively on the presence and nature of the multitudinous choice of impurities, counter-ions, and ligands. From this perspective, the MX class of materials are very good prospects for sensors that would be able to detect, for instance, minute traces of pollutants, smog particles and corrosive chemicals present in the air. We intend in future publications to describe our studies of the mixed-halide and mixed metal-alloy MX systems; as well as the influence of charge off the chain (e.g., from counter-ions or dopantions), extensions to MMX materials, and interchain coupling effects. Studies of the EPR, Raman, and ir signatures are in progress.[56] We will also use our molecular-dynamics and other techniques to probe photoexcitation and decay, including nonlinear optical coefficients (which are expected to be large for these anisotropic systems[60]) and photoluminescence. These properties may well set directions for device applications in this fascinating class of novel, strongly correlated, low-dimensional electronic materials.

ACKNOWLEDGMENTS

We would like to thank the many people who have collaborated in this research effort, including R.C. Albers, M. Alouani, M. Aronson, C. Boyle, S. Conradson, R.J. Donohoe, P.J. Hay, S.C. Huckett, S. Marianer, R.J. Martin, J. Reichl, H. Röder, B.I. Swanson, D. Tait, and L. Worl; as well as thank, among others, D. Baeriswyl, H. Büttner, D.K. Campbell, M. Haruki, K. Iwano, M. Kurita, S. Mazumdar, T. Mitani, K. Nasu, X. Sun, A. Terai, and Y. Wada for useful discussions. Work of S.R.P. was supported by the U.S. DOE BES-MS under Contract No. W-31-109-Eng-38. Work at LANL was supported by the U.S. DOE—Office of Basic Energy Sciences. We are also happy to acknowledge the Centers for Materials Science and Nonlinear Studies for computational support at Los Alamos National Laboratory. Travel funds for J.T.G. for collaborative research were provided in part by the Estate of Elsie G. Hall. J.T.G. wishes to acknowledge the hospitality of the Physikalisches Institut, Universität Bayreuth, where parts of the present work were done. J.T.G. and A.R.B. acknowledge the hospitality of the Physics Department of the University of Tokyo and the Institute for Molecular Science in Okazaki, where extensive discussions on this subject of mutual interest, MX chains, were held.

APPENDIX A: MOLECULAR RELAXATION AND MOLECULAR-DYNAMICS TECHNIQUE

In this appendix we describe the HF adiabatic molecular-relaxation and molecular-dynamics techniques used in this work.

A similar molecular-dynamics technique was previously used to study dynamics in polyacetylene.[38] The adiabatic (Born-Oppenheimer) approximation assumes that the motion of ions is described by well-defined trajectories following Newton's law. This approximation is valid when the Fermi velocity is much larger than the sound velocity. Given that the adiabatic approximation is in-

deed valid (which is tested in paper II, but is assumed to be valid throughout this paper) the equation of motion for the ions is then

$$M_n \ddot{y}_n = F_n \ , \tag{A1}$$

where F_n is the time-dependent effective force acting on the nth ion, arising from occupied electronic states and from the harmonic lattice interactions. Note that the $K_{MM} \to \infty$ limit corresponds to freezing the M atoms.

The force on the ions is generated from the potential

$$V(y_n) = E_0(y_n) + \tfrac{1}{2}K\sum \Delta_n^2 + \tfrac{1}{2}K_{MM}\sum_n (\Delta_{2n} + \Delta_{2n+1})^2 \tag{A2}$$

$$= V_e(y_n) + V_{\rm ph}(y_n) \ , \tag{A3}$$

recalling $\Delta_l = y_{n+1} - y_n$. The term $E_0(y_n)$, the electronic energy for a given ion configuration $\{y_n\}$, can be calculated as the sum of the occupied one-electron energies:

$$E_0(y_n) = \sum f_{\nu,\sigma}\varepsilon_{\nu,\sigma}. \tag{A4}$$

Here $f_{\nu,\sigma}$ is the occupation of the state ν with spin σ and the sum is over all occupied states. The problem is now to find the one electron energies, given an ion configuration $\{y_n\}$, a total chain length N and the number of electrons in the system. The one electron energies can be found by direct diagonalization of the $N \times N$ Hamiltonian. Once the potential $V(y_n)$ is known, the force F_n is found as a functional derivative

$$F_n = -\frac{\delta V(y_n)}{\delta y_n}. \tag{A5}$$

Dissipation or external electric fields may be added if desired.

In molecular *relaxation* the new atomic configuration at the $(k+1)$st time step is determined by

$$y_n^{k+1} = y_n^k + \gamma F_n/M_n \tag{A6}$$

if this results in a lowering of the energy of the system, and

$$y_n^{k+1} = y_n^k \tag{A7}$$

otherwise. The parameter γ is arbitrary and may be changed through the relaxation so as to most rapidly decrease the total energy of the system. The relaxation is complete when the forces on *all* the unconstrained ions in the system have reached a small predetermined value. Similarly, the new atomic configuration may be determined from the "self-consistency" condition

$$F_{\rm ph}(\tilde{y}_n^{k+1}) + F_e(y_n^k) = 0 \tag{A8}$$

and

$$y_n^{k+1} = \gamma\tilde{y}_n^{k+1} + (1-\gamma)y_n^k \ . \tag{A6'}$$

Again, the parameter γ may be varied to improve convergence. Our experience with the self-consistent method has shown that $\gamma \simeq 1 - 1.3$ is usually fastest.

In molecular dynamics, Eq. (A1) is integrated by the standard Verlet algorithm[61] (a second-order central-difference scheme). If we discretize time in steps Δt, we have from Eq. (A1):

$$y_n^{k+1} - 2y_n^k + y_n^{k-1} = (\Delta t)^2\frac{F_n^k}{M_n} \ . \tag{A9}$$

The Verlet scheme is very efficient and quite accurate. The energy is typically conserved to within 0.5% with no significant systematic drift. A higher-order predictor-corrector scheme would presumably be more accurate but would also require substantially more computer time and storage. The Beeman algorithm,[62] which has also been used to some extent in conventional molecular-dynamics calculations, has a slightly different definition of the velocity, but can be shown[63] to produce the same trajectories as Eq. (A7); it is however more expensive to compute.

In addition to the already mentioned parameters, we have used $\Delta t = 10^{-15}$sec and $\delta y_n = 0.001$ Å throughout this study.

APPENDIX B: DERIVATION OF EFFECTIVE ONE-BAND PARAMETERS

Since effective one-band models have been widely used, both in the MX chain literature[9,31] and for the related 2D models of the cuprate HTSC,[64] it is important to test just how well calculations in such one-band models agree with the full two-band results.

An effective one-band model can be derived in several ways. The most straightforward (standard) way is to expand in e_0, keeping only the states with energy near $+e_0$ and only the lowest order correction terms. From the Hamiltonian (1), we see that for states near e_0 (M states) the eigenvalue equations are

$$(E - e_0)\psi_{2n} = (-t_0 + \alpha\Delta_{2n})\psi_{2n+1} + (-t_0 + \alpha\Delta_{2n-1})\psi_{2n-1} - \beta_M(\Delta_{2n} + \Delta_{2n-1})\psi_{2n}, \tag{B1}$$

$$[E + e_0 + \beta_X(\Delta_{2n+1} + \Delta_{2n})]\psi_{2n+1} = (-t_0 + \alpha\Delta_{2n+1})\psi_{2n+2} + (-t_0 + \alpha\Delta_{2n})\psi_{2n} \simeq (2e_0)\ \psi_{2n+1}. \tag{B2}$$

Substituting Eq. (B2) and the equivalent of Eq. (B2) for ψ_{2n-1} into Eq. (B1), we see that the effective one-band parameters are (scheme 1)

$$t^{1b} = t_0\frac{t_0}{2e_0} \ ; \tag{B3a}$$

$$\alpha^{1b} = \alpha\frac{t_0}{2e_0} \ ; \tag{B3b}$$

$$\beta^{1b} = \beta_M + \frac{\alpha t_0}{e_0} \ ; \tag{B3c}$$

$$K^{1b} = K \ ; \tag{B3d}$$

$$U^{1b} = U \ . \tag{B3e}$$

We note that for the one-band model,[9] the CDW and BOW phase boundary is at $\beta^{1b}/\alpha^{1b}=2$ (when the rest of the parameters are fixed). In fact, this transformation maps the entire $\beta>0, e_0>0$ one-band phase diagram into the CDW portion of the two-band phase diagram, in agreement with the experimental lack of BOW complexes. For PtCl parameters of Table II, this yields an effective β^{1b}/α^{1b} of 2.1, putting it well into the CDW portion of the one-band phase diagram, in agreement with its strongly distorted experimental geometry. However, when the self-consistent calculation is performed, from Table VI one sees that these parameters give a value for the lattice distortion which is much too large, in disagreement with the assumption in the expansion that $\Delta^{1b}=\Delta$. If we constrain the distortion and determine K (scheme 1'), we still find an optical gap that is more than a factor of 2 too large, as shown in Table VI. One can also easily keep higher-order terms in Δ and e_0, yielding (scheme 2)

$$t^{1b}=t_0\frac{t_0}{2\epsilon}\left(1-\frac{\alpha^2\Delta^2}{t_0^2}\right); \tag{B4a}$$

$$\alpha^{1b}=\alpha\frac{t_0}{2\epsilon}; \tag{B4b}$$

$$\beta^{1b}=\beta_M+\frac{\alpha t_0}{\epsilon}; \tag{B4c}$$

$$K^{1b}=K; \tag{B4d}$$

$$U^{1b}=U; \tag{B4e}$$

where

$$\varepsilon=\frac{e_0+\sqrt{e_0^2+4(t_0^2-\alpha^2\Delta^2)}}{2}.$$

A comparison of energy levels is shown in Fig. 23 for the PtCl parameters of Table II. The above discussion implies that for parameters in the experimentally relevant range, it is necessary to keep the correction terms even for PtCl, where e_0 is relatively large. Note that although the bandwidths are now roughly in agreement with the underlying two band model, the self-consistent charge density and lattice distortion are not the same as in the two-band model, as shown in Table VI.

We have defined two additional effective one-band models where, rather than doing an expansion as above, we constrain the two-band and effective one-band values

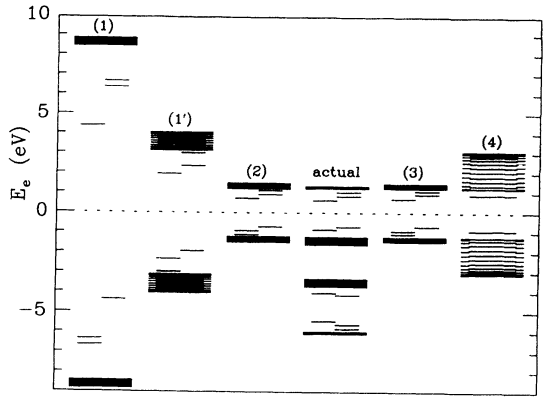

FIG. 23. Band structure derived from various effective one-band schemes as compared to the actual two-band values, for the PtCl parameters of Table II. The localized defect levels for electron (left) and hole (right) polarons predicted within each scheme are also shown.

of the optical gap and lattice distortion to be the same, yielding (for $U=0$)

$$\alpha^{1b}=\alpha\frac{t^{1b}}{t_0}; \tag{B5a}$$

$$\beta^{1b}=\frac{E_g}{4\Delta}; \tag{B5b}$$

$$K^{1b}=\frac{\beta^{1b}\delta\rho^{1b}}{\Delta}; \tag{B5c}$$

and t^{1b} is determined self-consistently from (again, for $U=0$):

$$\delta\rho^{1b}=\sum_{\substack{k,\sigma\\ \text{occ}}}\frac{4\beta^{1b}\Delta}{N|E^{1b}_{k,\sigma}|}. \tag{B5d}$$

Then either one can additionally constrain the spring constant K to be the same (scheme 3):

$$K^{1b}=K \tag{B6}$$

(so that $\delta\rho^{1b}=K\Delta/\beta^{1b}$), or constrain the charge density to be the same (scheme 4)

$$\delta\rho^{1b}=\delta\rho. \tag{B7}$$

A comparison of these energy levels is also shown in

TABLE VI. Optical gap, lattice distortion amplitude, and charge-density-wave amplitude derived from various effective one-band schemes (see text) as compared to the actual two-band values, for the PtCl parameters of Table II.

	(1)	(1')	(2)	(3)	(4)	Actual
t^{1b}	1.28	1.28	0.43	0.38	1.42	
α^{1b}	1.98	1.98	1.01	0.58	2.19	
β^{1b}	4.11	4.11	2.17	1.61	1.61	
K^{1b}	3.91	9.47	7.05	3.91	2.54	
E_g	16.9	6.25	2.41	2.45	2.54	2.45
Δ	1.03	0.38	0.28	0.38	0.38	0.38
$\delta\rho_M$	0.98	0.88	0.90	0.92	0.60	0.60

Fig. 23 and the structural information in Table VI for the PtCl parameters of Table II. From Fig. 23, it is obvious that the band structure agrees best when we constrain K rather than $\delta\rho$.

The final test of which scheme is the best one-band approximation is a comparison of defect levels. Thus in Fig. 23, we also show the predicted locations of the localized electron and hole polaron levels for each scheme. The one-band models all have electron levels symmetric with the hole levels reflected about the center of the gap (fixed to be at $E_e = 0$ in the figure). Additional symmetry-breaking terms would have to be added to the Hamiltonian if the asymmetry of the two-band electron and hole absorptions were to be retained. In the limit $e_0 \rightarrow \infty$, the answer should be independent of the scheme. For realistic parameter values it appears that scheme (2) — the expansion in e_0 with higher-order terms — and scheme (3) — the forced fit of the one-band optical gap, dimerization and spring constant — give good agreement for the lattice distortion, band structure, and defect absorptions with the actual two-band calculation. It is important to note this implies that for the effective one-band model

$$\delta\rho^{1b} \neq \delta\rho \ .$$

Hence, if one wants to investigate the effects of the Hubbard terms in the effective one-band model, the Hubbard terms must also be renormalized, e.g.,

$$U^{1b} = U_M \left(\delta\rho/\delta\rho^{1b}\right)^2 \ . \tag{B8}$$

[1] M.B. Robin and P. Day, in *Advances in Inorganic Chemistry and Radiochemistry*, edited by H.J. Emeleus (Academic, New York, 1967), Vol. 10, p. 247; P. Day, in *Low Dimensional Cooperative Phenomena*, edited by H.J. Keller (Plenum, New York, 1974), p. 191; H.J. Keller, in *Extended Linear Chain Compounds*, edited by J.S. Miller (Plenum, New York, 1982), Vol. 1, p. 357.

[2] H. Toftlund and O. Simonsen, Inorg. Chem. **23**, 4261 (1984).

[3] K. Toriumi, Y. Wada, T. Mitani, S. Bandow, M. Yamashita, and Y. Fujii, J. Am. Chem. Soc. **111**, 2341 (1989); K. Toriumi *et al.*, Mol. Cryst. Liq. Cryst. **181**, 333 (1990); H. Okamoto, K. Toriumi, T. Mitani, and M. Yamashita, Phys. Rev. B **42**, 10 381 (1990).

[4] R. J. H. Clark, in *Advances in Infrared and Raman Spectroscopy*, edited by R. J. H. Clark and R. E. Hester (Wiley, New York, 1984), Vol. 11, p. 95; R.J.H. Clark and V.B. Croud, in *Organic and Inorganic Low-Dimensional Crystalline Materials*, edited by P. Delhaes and M. Drillon (Plenum, New York, 1987).

[5] B. I. Swanson, M. A. Stroud, S. D. Conradson, and M. H. Zeitlow, Solid State Commun. **65**, 1405 (1988); M.A. Stroud, S.A. Ekberg, and B.I. Swanson, Chem. Mater. **2**, 366 (1990).

[6] J.B. Torrance, J.E. Vasquez, J.J. Mayerle, and V.Y. Lee, Phys. Rev. Lett. **46**, 253 (1981).

[7] M.J. Rice, C.B. Duke, and N.O. Lipari, Solid State Commun. **17**, 1089 (1975).

[8] V.J. Emery, Phys. Rev. Lett. **58**, 2794 (1987); **65**, 1076 (1990); J.T. Gammel, I. Batistić, A.R. Bishop, E.Y. Loh, Jr., and S. Marianer, Physica B **163**, 458 (1990).

[9] D. Baeriswyl and A.R. Bishop, Phys. Scr. **T19**, 239 (1987); J. Phys. C **21**, 339 (1988).

[10] R.E. Peierls, *Quantum Theory of Solids* (Clarendon, Oxford, 1955), p. 108.

[11] I. Batistić, J. Tinka Gammel, and A. R. Bishop, Phys. Rev. B **44**, 13 228 (1991).

[12] S.M. Weber-Milbrodt, J. Tinka Gammel, A.R. Bishop, and E.Y. Loh, Jr., following paper, Phys. Rev. B **45**, 6435 (1991) (paper II).

[13] T. M. Rice and L. Sneddon, Phys. Rev. Lett. **47**, 689 (1981); C. M. Varma, *ibid.* **61**, 2713 (1988).

[14] J. Liu and G.-X. Yang (unpublished); L.V. Interante, K.W. Browall, and F.D. Bundy, Inorg. Chem. Acta **13**, 1158 (1974).

[15] W.-P. Su, J.R. Schrieffer, and A.J. Heeger, Phys. Rev. Lett. **42**, 1698 (1979); Phys. Rev. B **22**, 2209 (1980); **28**, 1138(E) (1983).

[16] S. Kurita and M. Haruki, Synth. Metals **29**, F129 (1989); M. Tanaka and S. Kurita, J. Phys. C **19**, 3019 (1986).

[17] N. Kuroda, M. Sakai, M. Suezawa, Y. Nishina, and K. Sumino, J. Phys. Soc. Jpn. **59**, 3049 (1990).

[18] M. Haruki and S. Kurita, Phys. Rev. B **39**, 5706 (1989).

[19] S.C. Huckett, E. Garcia, J.R. Laia, D. Carroll, and B.I. Swanson, Synth. Metals **41-43**, 2777 (1991); S.C. Huckett, C.A. Arrington, C.J. Burns, D.L. Clark, and B.I. Swanson, *ibid.* **41-43**, 2769 (1991).

[20] Y. Wada, T. Mitani, K. Toriumi, and M. Yamashita, J. Phys. Soc. Jpn. **58**, 3013 (1989).

[21] H. Tanino, H. Oyagi, M. Yamashita, and K. Kobayashi, Solid State Commun. **53**, 953 (1985); M. Tanaka, S. Kurita, Y. Okada, T. Kojima, and Y. Yamada, Chem. Phys. **96**, 343 (1985); Y. Wada, T. Mitani, M. Yamashita, and T. Koda, Synth. Metals **19**, 907 (1987).

[22] S. Kurita, M. Haruki, and K. Miyagawa, J. Phys. Soc. Jpn. **57**, 1789 (1988); L. Degiorgi, P. Wachter, M. Haruki, and S. Kurita, Synth. Metals **29**, F137 (1989); Phys. Rev. B **40**, 3285 (1989); **41**, 573 (1990).

[23] R. Donohoe, D. Tait, and B.I. Swanson, Chem. Mater. **2**, 315 (1990); R.J. Donohoe, R.B. Dyer, and B.I. Swanson, Solid State Commun. **73**, 521 (1990); S.C. Huckett, R.J. Donohoe, L.A. Worl, A.D.F. Bulou, C.J. Burns, J.R. Laia, D. Carroll, and B.I. Swanson, Chem. Mater. **3**, 123 (1991); S.D. Conradson, R.F. Dillinger, B.I. Swanson, R.J.H. Clark, and V.B. Croud, Chem. Phys. Lett. **135**, 463 (1987); R.J. Donohoe, L.A. Worl, C.A. Arrington, and B.I. Swanson, J. Phys. C (to be published).

[24] S.C. Huckett, R.J. Donohoe, L.A. Worl, A.D.F. Bulou, C.J. Burns, and B.I. Swanson, Synth. Metals **41-43**, 2773 (1991); B.I. Swanson, R.J. Donohoe, L.A. Worl, A.D.F. Bulou, C.A. Arrington J.T. Gammel, A. Saxena, and A.R. Bishop, Mol. Cryst. Liq. Cryst. **194**, 43 (1991).

[25] See the several contributions on MX chains in the Proceedings of the International Conference on the Science and

Technology of Synthetic Metals (ICSM 1990), Tübingen, West Germany, 1990 [Synth. Metals **41-43** (1991)].

[26] R.C. Albers, Synth. Metals **29**, F169 (1989); R.C. Albers, M. Alouani, J.M. Wills, and M. Springborg, *ibid.* **41/43**, 2739 (1991); M. Alouani and R.C. Albers (unpublished).

[27] The unpublished *ab initio* calculations were performed variously by C. Boyle, R. L. Martin, and P. J. Hay.

[28] M.J. Rice and E.J. Mele, Phys. Rev. Lett. **49**, 1455 (1982).

[29] M. Yamashita, I. Murase, Y. Wada, T. Mitani, and I. Ikemoto, Bull. Chem. Soc. Jpn. **58**, 2336 (1985).

[30] A.R. Bishop, J. Tinka Gammel, and S.R. Phillpot, Synth. Metals **29**, F151 (1989); J. Tinka Gammel, S.M. Weber-Milbrodt, E.Y. Loh, Jr., and A.R. Bishop, *ibid.* **29**, F161 (1989); A.R. Bishop, J. Tinka Gammel, E.Y. Loh, Jr., S.R. Phillpot, and S.M. Weber-Milbrodt, in Proceedings of the NATO Advanced Research Workshop on Interacting Electrons in Reduced Dimensions, Torino, Italy, Vol. 213 of *NATO Advanced Study Institute, Series B: Physics*, edited by D. Baeriswyl and D. K. Campbell (Plenum, New York, 1991).

[31] K. Nasu, J. Phys. Soc. Jpn. **50**, 235 (1981); **52**, 3865 (1983); **53**, 302 (1984); **53**, 427 (1984); **54**, 1933 (1985); J. Lumin. **38**, 90 (1987); K. Nasu and Y. Toyozawa, J. Phys. Soc. Jpn. **51**, 2098 (1982); **51**, 3111 (1982); A. Mishima and K. Nasu, Synth. Metals **29**, F175 (1989).

[32] Y. Ichinose, Solid State Commun. **50**, 137 (1984).

[33] Y. Onodera, J. Phys. Soc. Jpn. **56**, 250 (1987).

[34] I. Batistić, X. Z. Huang, and A. R. Bishop (unpublished).

[35] See, e.g., the section on Lanczos diagonalization in S. Pissanetsky, *Sparse Matrix Technology* (Academic, London, 1984).

[36] V. Waas, J. Voit, and H. Büttner, Synth. Metals **27**, A21 (1988).

[37] J. Weinrach, M. Hawley, A. P. Sattelberger, and B.I. Swanson, Solid State Commun. **77**, 853 (1991).

[38] S.R. Phillpot, D. Baeriswyl, A. R. Bishop, and P. S. Lomdahl, Phys. Rev. B **35**, 7533 (1987).

[39] J.C. Hicks and J. Tinka Gammel, Phys. Rev. Lett. **57**, 1320 (1986).

[40] In the $t_0 = \alpha = 0$ limit, one can label the configuration by the charge on each site. Thus, going from the left ground state configuration 2220 to the right ground-state configuration 2022, the K^+ centered on a $4n+1$ site would be

$$\cdots 2220\,2220\,2022\,2022 \cdots .$$

The K^+ centered on a $4n+3$ site would be

$$\cdots 2220\,2220\,2121\,2022 \cdots .$$

Clearly, the K^+ centered at $4n+1$ is the more localized case.

[41] K. Fesser, A. R. Bishop, and D. K. Campbell, Phys. Rev. B **27**, 4804 (1983).

[42] J.C. Hicks and Y.R. Lin-Liu, Phys. Rev. B **29**, 5641 (1984).

[43] One expects two intragap levels for polarons in one-band models. The third weakly localized level in the present case arises from the two-band nature of the model.

[44] Charge conjugation symmetry in the two-band model exists between a hole defect in a $\frac{1}{4}$-filled band and an electron defect in a $\frac{3}{4}$-filled band, rather than between electron and hole defects around the Fermi surface, in contrast to the case in $\frac{1}{2}$-filled one-band models.

[45] We have calculated the absorption spectra and lattice distortion for the triplet case in this paper. For $U=0$, the lattice distortion and single particle electronic energies for the singlet neutral bipolaron will be identical, though the singlet will have additional allowed optical transitions between the localized levels.

[46] J. Tinka Gammel and J.C. Hicks, Phys. Rev. B **32**, 7020 (1985).

[47] M. J. Rice, A. R. Bishop, and D. K. Campbell, Phys. Rev. Lett. **51**, 2136 (1983); S. R. Phillpot, M. J. Rice, A. R. Bishop, and D.K. Campbell, Phys. Rev. B **36**, 1735 (1987).

[48] A.R. Bishop, D.K. Campbell, P.S. Lomdahl, B. Horovitz, and S.R. Phillpot, Phys. Rev. Lett. **52**, 671 (1984).

[49] B. Horovitz, A. R. Bishop, and S. R. Phillpot, Phys. Rev. Lett. **60**, 2210 (1988); S.R. Phillpot, A.R. Bishop, and B. Horovitz, Phys. Rev. B **40**, 1839 (1989).

[50] Hole polarons have similar dynamics, the specifics we defer to a later publication, Ref. 51.

[51] A. Saxena, J.T. Gammel, and A.R. Bishop (unpublished).

[52] There have been no systematic studies of doping. These materials are self-doped in the range of a few percent in their synthesis, as determined from the susceptibility (see Ref. 57).

[53] R. J. Donohoe, S. A. Ekberg, C. D. Tait, and B. I. Swanson, Solid State Commun. **71**, 49 (1989).

[54] J.T. Gammel, R.J. Donohoe, A.R. Bishop, and B.I. Swanson, Phys. Rev. B **42**, 10 566 (1990).

[55] S. Love (private communication).

[56] I. Batistić, A. Saxena, A. R. Bishop, and M. Alouani (unpublished); A. Bulou, R.J. Donohoe, and B.I. Swanson, J. Phys. Condens. Matter **3**, 1709 (1991).

[57] W.E. Hatfield and L.W. ter Haar, Ann. Rev. Mater. Sci. **12**, 177 (1982); M. Haruki and P. Wachter, Proceedings of the International Conference on Low Temperature Physics, Brighton, 1990 [Physica B **165**, 891 (1990)]; M. Aronson *et al.* (unpublished).

[58] R.J. Donohoe (private communication).

[59] S. D. Conradson *et al.* (unpublished) (PtBr); R. J. Donohoe *et al.* (unpublished) (PtCl).

[60] Y. Wada and M. Yamashita, Jpn. J. Appl. Phys. **29**, 2744 (1991).

[61] L. Verlet, Phys. Rev. **159**, 98 (1967).

[62] D. Beeman, J. Comput. Phys. **20**, 130 (1976).

[63] R.W. Hockney and J.W. Eastwood, *Computer Simulation Using Particles* (McGraw-Hill, New York, 1981).

[64] F.C. Zhang and T.M. Rice, Phys. Rev. B **37**, 3759 (1988).